Disrupted endosomal trafficking of the Vangl-Celsr polarity complex underlies congenital anomalies in trachea-esophageal morphogenesis

Nicole A. Edwards[1*], Adhish Kashyap[1], Alissa Warren[1], Zachary N. Agricola[1,2], Alan P. Kenny[2], Yufeng Shen[4,5], Wendy K. Chung[6,7], Aaron M. Zorn[1,3,8*]

[1]Center for Stem Cell and Organoid Medicine (CuSTOM), Perinatal Institute, Division of Developmental Biology, Cincinnati Children's Hospital Medical Center, Cincinnati, OH, 45208 USA

[2]Perinatal Institute, Division of Neonatology, Cincinnati Children's Hospital Medical Center, Cincinnati, OH, 45208 USA

[3]University of Cincinnati, College of Medicine, Cincinnati, OH, USA

[4]Department of Systems Biology, Columbia University Irving Medical Center, New York, NY, 10032 USA

[5]Department of Biomedical Informatics, Columbia University Irving Medical Center, New York, NY, 10032 USA

[6]Department of Pediatrics, Boston Children's Hospital, Harvard Medical School, Boston, MA, 02115 USA

[7]Departments of Pediatrics and Medicine, Columbia University Irving Medical Center, New York, NY

[8]Lead contact

*Correspondence: aaron.zorn@cchmc.org, nicole.edwards@cchmc.org

Summary

Disruptions in foregut morphogenesis can result in life-threatening conditions where the trachea and esophagus fail to separate properly, such as esophageal atresia (EA) and tracheoesophageal fistulas (TEF). The developmental basis of these congenital anomalies is poorly understood, but recent genome sequencing reveals that *de novo* variants in intracellular trafficking genes are enriched in EA/TEF patients. Here we show that mutation of orthologous genes in *Xenopus* disrupts trachea-esophageal separation similar to EA/TEF patients. We show that the Rab11a recycling endosome pathway is required to localize Vangl-Celsr polarity complexes at the cell surface where opposite sides of the common foregut tube fuse. Partial loss of endosome trafficking or the Vangl/Celsr complex disrupts epithelial polarity and cell division orientation. Mutant cells accumulate at the fusion point, fail to downregulate cadherin, and do not separate into distinct trachea and esophagus. These data provide new insights into the mechanisms of congenital anomalies and general paradigms of tissue fusion during organogenesis.

Introduction

Esophageal atresia (EA) and tracheoesophageal fistulas (TEF), which affect approximately 1 in 3000 newborns, are life-threatening congenital anomalies that arise when the embryonic foregut does not separate correctly into distinct trachea and esophageal tubes[1-3]. This results in esophageal discontinuity (EA) and/or a pathological connection between the trachea and esophagus (TEF). Rarer are laryngeal-tracheal-esophageal-clefts where in some extreme cases the foregut fails to separate along its entire length, essentially resulting in an extended complete TEF[4]. Roughly half of EA/TEF patients also have variably penetrant co-occurring anomalies in other organs including gastrointestinal, pulmonary, cardiovascular, renal and the central nervous system, suggesting undefined syndromes [5,6]. The genetic etiology of tracheoesophageal anomalies is poorly understood and is associated with spontaneous *de novo* variants, chromosomal rearrangements, copy number variation, indels, and single nucleotide changes in affected newborns[1,7]. Known variants only account for 10-15% of cases world-wide with the remaining having no identified risk gene. Even when the causative variants are known, why they result in tracheoesophageal anomalies is unclear since the cellular mechanisms governing foregut morphogenesis are poorly understood.

Tracheoesophageal morphogenesis begins when the foregut endoderm is patterned along the dorsal-ventral axis by an evolutionarily conserved Hedgehog-Wnt-Bmp signaling network

resulting in dorsal Sox2+ esophageal progenitors and ventral Nkx2-1+ respiratory progenitors[8-11]. After patterning, the foregut constricts at the midline and a population of epithelial cells on either side of the foregut tube that express both dorsal and ventral markers (Sox2/Nkx2-1/Islet1) come together and adhere forming a transient epithelial bilayer[12,13]. Epithelial cells at the fusion point then progressively lose adhesion to one another and integrate into either the ventral or dorsal foregut as the surrounding Foxf1+ splanchnic mesoderm invades between the nascent trachea and esophagus[13]. Thus, the single foregut epithelial tube fuses, reorganizes its cellular junctions at the luminal/apical surface, then undergoes fission with coordinated cell rearrangements to reconnect the epithelia into two separate tubes.

How cell signaling pathways and transcription factors regulate these cellular processes is poorly understood. Similar epithelial fusion events occur in other tissues including the heart, oral palate, eyes, and neural tube; organ systems that are frequently disrupted in complex EA/TEF patients, suggesting common biological mechanisms[14]. Studies in these other organs indicate that dynamic changes in tissue and cell polarity are necessary for proper morphogenesis [14,15]. For example, vertebrate neural tube closure and morphogenesis of the *Drosophila* retina both require the spatial-temporal coordination of apical-basal and planar cell polarity (PCP) proteins, but how polarity and junctional proteins are localized and coordinated to regulate epithelial fusion and remodeling is unclear [16-19].

We recently found in *Xenopus* that downstream of Hedgehog signaling, Rab11+ recycling endosomes somehow regulate tracheoesophageal morphogenesis [13]. Rab11 is a key small GTPase in the recycling endosome pathway that cells use to transport newly synthesized proteins from the Golgi to plasma membrane and to change the composition of specific plasma membrane domains by internalizing receptors and other cell surface proteins [20]. How recycling endosomes regulate foregut epithelial remodeling was unclear, but intriguingly, whole genome sequencing analysis revealed that EA/TEF patients with complex multi-organ phenotypes are enriched for potentially damaging *de novo* variants in genes related to endocytosis and intracellular trafficking [21]. These two independent observations led us to test the hypothesis that endosome trafficking is a crucial morphogenetic bottleneck in tracheoesophageal separation and to define the underlying mechanisms.

Here we demonstrate that the Rab11a recycling endosome pathway is required upstream of the Vangl-Celsr PCP complex for proper fission of the foregut tube. Mechanistically, Rab11a

93 localizes the transmembrane protein Vangl2 specifically to the midline luminal cell surface
94 where opposite sides of the foregut touch, upregulate cadherin, and adhere to one another to
95 form the transient epithelial bilayer. Rab11a and Vangl-Celsr complexes enriched at the contact
96 surface appear to confer an "apical memory" essential to maintain the transient bilayer and its
97 subsequent resolution. A partial loss of 1) core endosome trafficking components, 2) orthologs
98 of EA/TEF patient risk genes, or 3) the Vangl-Celsr proteins disrupts cell polarity and the
99 orientation of cell division in the transient bilayer. Mutant cells accumulate in a disorganized
100 septum, fail to downregulate cadherin, and do not properly separate into distinct trachea and
101 esophagus. This unexpected Vangl/Celsr activity is distinct from their well-known Wnt/PCP role
102 in orienting cells within the plane of the epithelium and is an unusual twist on their typical
103 function in defining apical-basal epithelial polarity. Together these results indicate that failure to
104 maintain localized endosome-mediated epithelial polarity during foregut morphogenesis may be
105 a common disease mechanism underlying EA/TEF in many patients and may have broad
106 implications for tissue fusion events in the development of other organs.
107
108 **Results**
109 **Variants in endosome pathway genes are enriched in EA/TEF patients and cause TEF in**
110 ***Xenopus***
111 Genome sequencing recently identified a cohort of complex EA/TEF patients with potentially
112 gene damaging and missense *de novo* heterozygous variants in 55 genes involved in
113 intracellular trafficking and endocytosis [21]. A meta-analysis of experimentally validated protein-
114 protein interactions from the STRING database [22] revealed that many of the proteins encoded
115 by patient risk genes interact with core recycling endosome components (Figure 1A), supporting
116 recent evidence that this pathway has an important role in tracheoesophageal morphogenesis
117 [13]. To determine if these patient variants were likely to be causative risk alleles, we mutated
118 orthologous genes in *Xenopus tropicalis* using F0 CRISPR-Cas9 gene editing, which
119 recapitulates the *de novo* variants in newborn patients. We designed CRISPR guide RNAs
120 (gRNAs) to induce indel mutations early in the coding sequence to disrupt protein function, and
121 injected Cas9-gRNA complexes into one cell-stage embryos. After of three days of
122 development, embryos were genotyped, and tracheoesophageal morphogenesis was assayed
123 by immunostaining and confocal microscopy (Figure 1B). If the embryos had EA/TEF-like
124 phenotypes, then the patient variant is likely a risk variant.
125

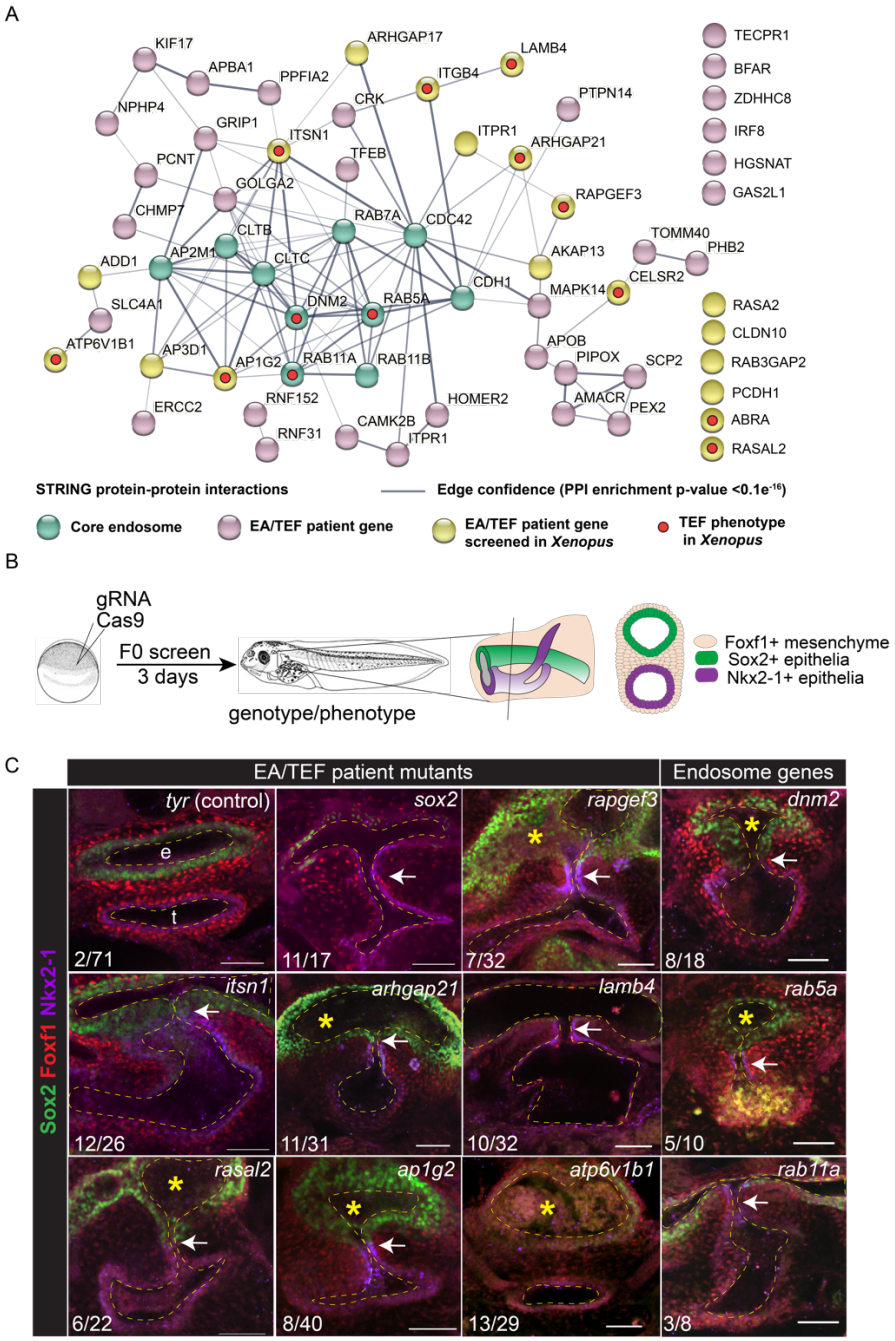

Figure 1. Mutating EA/TEF patient endosome trafficking genes causes TEDs in *Xenopus*. A) STRING Database interactome of endosome-related proteins with potentially pathogenic variants identified in EA/TEF patients together with a curated list of core endosome pathway proteins and putative protein cargo. B) Experimental design of F0 CRISPR-Cas9 *X. tropicalis* mutagenesis screen to validate candidate risk genes. C) Confocal images of CRISPR-Cas9 *X. tropicalis* F0 mutants at NF44 stained for Sox2 (green), Foxf1 (red), and Nkx2-1 (purple). Hashed yellow lines indicate the trachea (t) and esophageal (e) lumens and arrows indicate trachea-esophageal fistulas. Asterisks indicate presence of esophageal dysmorphology. Numbers indicate the number of CRISPR mutant tadpoles with TEF compared to the total mutants screened. Scale bars are 50 µm.

We found that mutations in 10/19 orthologs of endosome-related patient risk genes (*abra, ap1g2, arhgap21, atp6v1b1, celsr2, itgb4, itsn1, lamb4, rapgef3* and *rasal2*) when mutated in *Xenopus* result in variably penetrant tracheoesophageal anomalies in *Xenopus* (Figure 1C and Table S1). This was also true for F0 mutations in the known EA/TEF risk gene *sox2* and mutations in genes encoding key GTPases in endosome trafficking: *dynamin-2* (*dnm2)*, which regulates vesicle formation at the cell surface, *rab5a*, which regulates early endosome trafficking, and *rab11a* involved in recycling endosomes that transports vesicles to the cell surface (Table S1). Genotyping of individual embryos revealed a 30-90% damaging indel rate, suggesting a significant loss of protein but not complete null mutants (Table S1 and Figure S1). In each case, the foregut was correctly patterned into a ventral Nkx2-1+ trachea domain and a dorsal Sox2+ esophageal domain with surrounding Foxf1+ mesenchyme, and the foregut underwent initial constriction at the midline with the walls of the foregut epithelia coming together. However, in many embryos the foregut failed to separate into distinct tubes and exhibited a persistent fistula (Figure 1C, arrows). Some patient genes (*rapgef3, arhgap21, rasal2, ap1g2, atp6v1b1*) when mutated also exhibited a dysmorphic esophagus ranging from stenosis to a thick multilayered epithelium with multiple or occluded esophageal lumens (Figure 1C, asterisks), consistent with EA in patients. These results demonstrate that endosome trafficking is required for tracheoesophageal morphogenesis in *Xenopus* and support the likelihood that variants in endosome-related genes may have caused EA/TEF in some patients.

Dynamic endosome localization and epithelial remodeling during foregut morphogenesis

To better understand the cellular mechanisms by which endosome trafficking regulates *Xenopus* foregut morphogenesis, we performed a detailed immunostaining analysis over the 24-hour period when the single foregut separates into distinct esophageal and tracheal tubes (Figure 2). At the onset of tracheoesophageal morphogenesis (stage NF37), the endodermal foregut tube is a typical apical-basal polarized pseudostratified columnar epithelium. Cdh1 (E-cadherin) is enriched in adherens junctions and along the basal-lateral cell borders, and tight junctions and apical polarity cell proteins like aPKC and Par3 are localized to the luminal/apical cell surface, whilst laminin lines the basal surface contacting the surrounding mesoderm (Figure 2A,E and Figure S2A-C). As the foregut constricts in the midline (stage NF37) and the opposing epithelia touch, apical proteins aPKC and Par3 are downregulated and Tjp1+ tight junctions are lost (Figure 2F,J and Figure S2D-G). This is coincident with an upregulation of Cdh1 at the

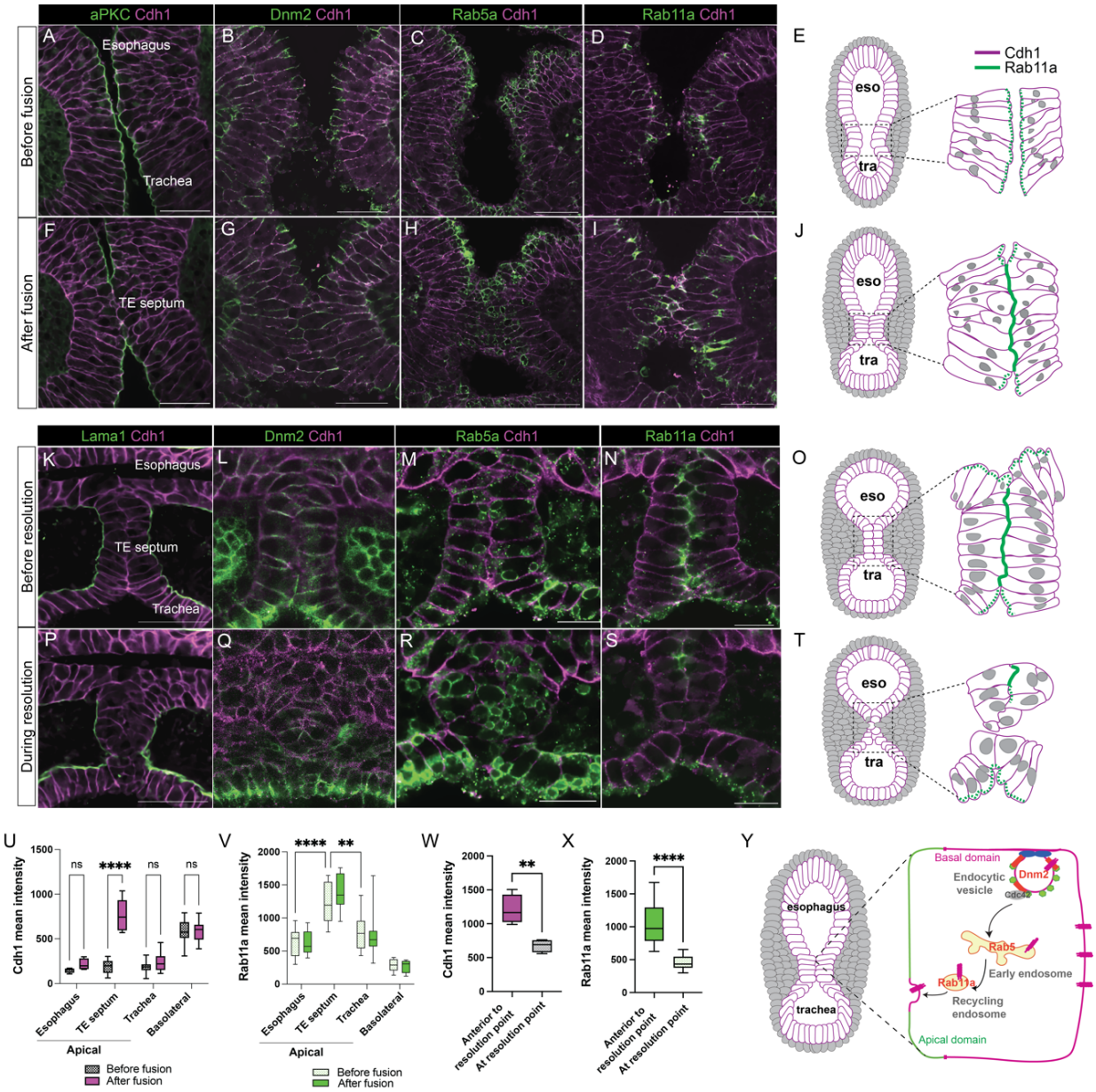

Figure 2. Dynamic endosome localization and epithelial remodeling during tracheoesophageal morphogenesis. A-J) Immunostaining of aPKC, Cdh1, Dnm2, Rab5a, and Rab11a in the NF37 foregut during epithelial fusion. K-T) Immunostaining of the NF41 foregut before and during resolution of the epithelial bilayer. E, J, O, T) Diagrams depicting the temporal-spatial dynamics of Cdh1 and Rab11a subcellular localization during tracheoesophageal morphogenesis. U) Quantification of Cdh1 immunostaining intensity in the membrane before and after fusion in the foregut (mean ± min/max, 2W-ANOVA, ****p<0.0001, n=4-6 embryos analyzed). V) Quantification of Rab11a immunostaining intensity before and after foregut fusion (mean ± min/max, 2W-ANOVA, ****p<0.0001, n=4-6 embryos analyzed). W) Quantification of Cdh1 signal intensity in the bilayer before and during resolution (mean ± min/max, Student's t-test, **p<0.01, n=4-6 embryos analyzed). X) Quantification of Rab11a signal intensity in the bilayer before and during resolution (mean± min/max, Student's t-test, **p<0.01, n=4-6 embryos analyzed). Y) A model of how endosome trafficking may mediate Cdh1 re-localization during epithelial fusion.

contact point (Figure 2F,U), which presumably helps mediate adhesion of the two sides and the formation of a well-organized, but transient, columnar epithelial bilayer by NF39 (Figure 2K, O, Figure S2J). After 12 hours, at NF41-42, columnar cells in the middle of the epithelial bilayer downregulate Cdh1, round up, lose attachment to their neighbors, and appear to integrate into either the trachea or esophagus as mesenchyme cells invade to complete separation of the foregut (Figure 2P,T,W, Figure S2K-L,O).

Co-staining for the endosome pathway GTPases Dnm2, Rab5a, and Rab11a revealed intriguing patterns of subcellular localization during this epithelial remodeling (Figure 2). Throughout the process of foregut fusion, all epithelial cells (dorsal, ventral, and midline) have Dnm2 enriched at the apical-lateral membrane and subapical Rab5a+ early endosome vesicles (Figure 2B-C,G,-H, Figure S2H-I). In contrast, the recycling endosome Rab11a only becomes robustly enriched at the luminal contact point where the two sides of the foregut epithelia touched (Figure 2D,I,J,V). Many Rab11a+ puncta at the contact point co-stain for Cdh1 with robust co-localization persisting at the adhesion surface between the two epithelial in the bilayer consistent with previous reports[13]. At NF41-42, when the epithelial bilayer progressively resolves, Rab11a and Cdh1 levels significantly drop as the columnar cells round up and lose attachment to their neighbors (Figure 2N,S,X). At this time Dnm2 is also observed in the mesenchyme surrounding septum, while Rab5a marks submembrane vesicular structures (Figure 2L-M,Q-R and Figure S2M-N). Collectively these analyses reveal dynamic localized endosomal trafficking during the epithelial remodeling that separates the trachea and esophagus (Figure 2Y).

Endosome trafficking is required for maintenance and resolution of a transient epithelial bilayer during tracheoesophageal morphogenesis

We next determined which of the epithelial remodeling events driving tracheoesophageal morphogenesis require endosome trafficking. A time course immunostaining of *dnm2*, *rab5a*, and *rab11a* mutant embryos showed that initial foregut constriction and epithelial fusion with downregulation of aPKC and upregulation of Cdh1 at the contact surface occurred normally (Figure 3A, Figure S3B-C). However, mutant embryos did not form or maintain an organized columnar epithelia bilayer between the presumptive trachea and esophagus. Rather, the mutant septa were disorganized and 4-6 cells wide with cells in the middle being round rather than columnar (Figure 3B,D). Moreover, at NF41 the mutant septum did not downregulate Cdh1 and

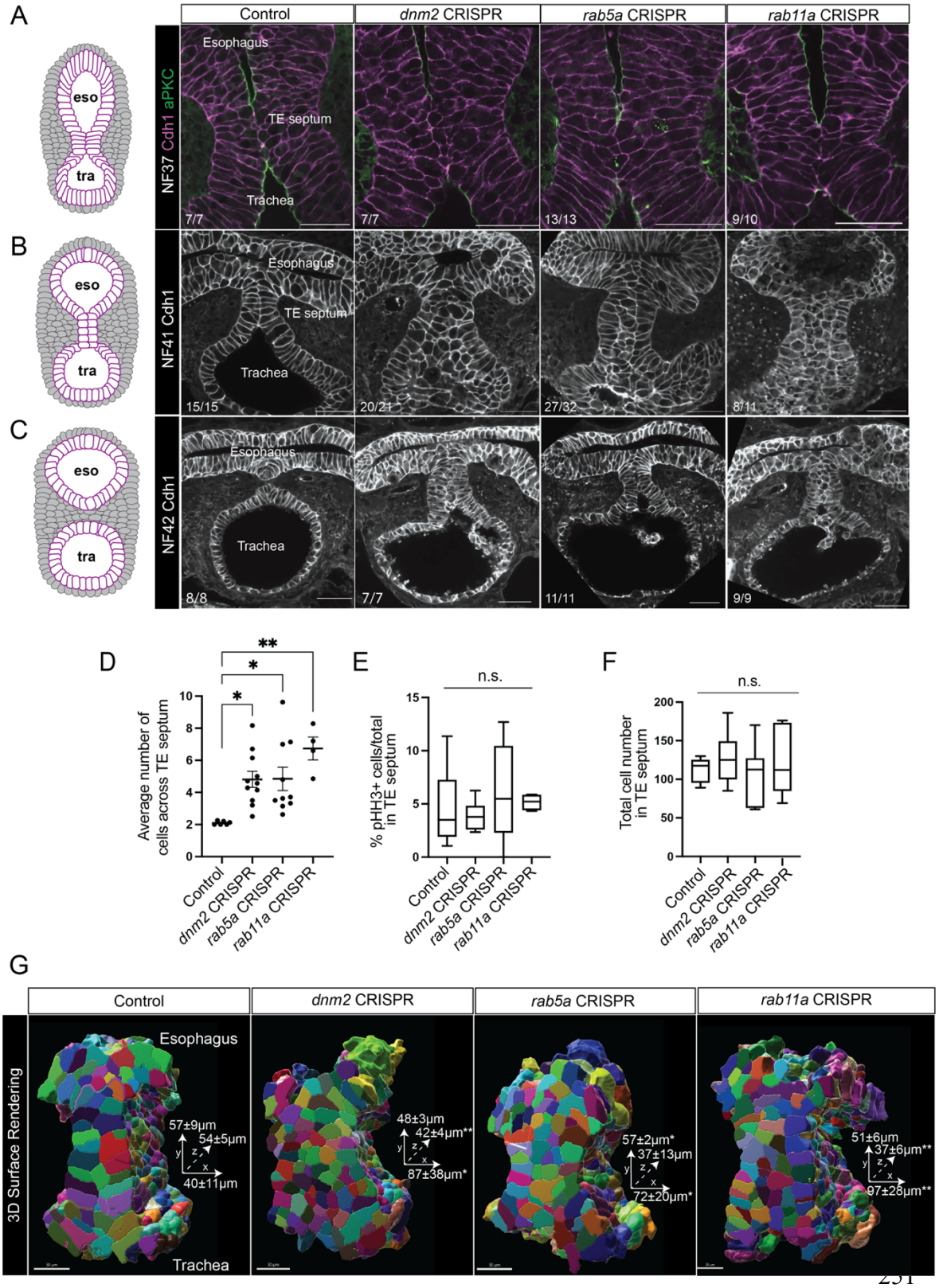

Figure 3. Disrupting endosome trafficking causes TEF in *Xenopus*. A) At NF37 the septum in *dnm2*, *rab5a*, and *rab11a* CRISPR mutants undergoes epithelial fusion and down regulate apical polarity proteins similarly to controls. B) At NF41 the epithelial bilayer in endosome mutants is disorganized compared to controls. C) *dnm2*, *rab5a*, and *rab11a* CRISPR mutants exhibit TEF.

Scale bars are 50 μm. D) The mutant epithelia septa have significantly more cells across the width of the tissue compared to controls (mean ± SEM, * $p<0.05$ 1W-ANOVA, ** $p < 0.01$, N=6-11 embryos). E) There are no significant (n. s.) differences in proliferation (pHH3+/total) or F) total cells in the septum of mutant embryos compared to controls (mean ± min/max, 1W-ANOVA, n=4-6 embryos). G) 3D surface renderings and measurements of the epithelial septum showing that mutants are significantly wider (x axis) and shorter in the rostral-caudal (z axis) axis compared to controls (mean length ± SEM, Student's t-test compared to control lengths, *$p<0.05$, **$p<0.01$, n=4-6 embryos per condition). Scale bars are 30 μm.

resolve into distinct trachea and esophageal tubes, but remained a disorganized epithelial mass, with frequent blisters, resulting in a blind ended fistula (Figure 3C, Figure S3D, Table S1).

A proportion of endosome mutants also exhibited a dysmorphic esophagus and occluded tracheal lumens (Figure 3B, Table S1). These results indicate that endosome trafficking is required to maintain an organized epithelial bilayer, and suggest that the accumulation of too many cells with persistent Cdh1 expression disrupts the resolution into distinct trachea and esophageal tubes.

To determine if the accumulation of cells was due to elevated cell proliferation, we quantified confocal Z-stacks of the entire foregut region and found that neither the total number of cells in the trachea-esophageal septum nor the rate of proliferation (phosphorylated histone H3 staining) was significantly increased in endosomal mutants compared to controls (Figure 3E-F). Three dimensional reconstructions demonstrated that the mutant septa were wider (x-axis) and shorter in the rostral-caudal axis (z-axis) compared to controls but were similar in the dorsal-ventral axis (y-axis) (Figure 3G). This indicates that mutant cells somehow accumulate across the width of the epithelia septum at the expense of fewer cells along the rostral-caudal extension of the separating trachea and esophagus.

Endosome trafficking controls the orientation of division in the foregut epithelial bilayer

Since polarized epithelial cells are known to divide into the plane of the tissue to maintain a single layer organization, we considered the possibility that in the mutant embryos, cells might aberrantly divide into the middle of the septum contributing to the cell build-up (Figure 4A). To assess the plane of cell division, we measured the angle of the mitotic spindle relative to the basal membrane in the septum of endosomal mutants and controls. While cells in the epithelial bilayer of control embryos divided into the plane of the epithelia as expected, with an average spindle orientation of 0-15°, *dnm2*, *rab5a,* and *rab11a* mutants exhibited a more random

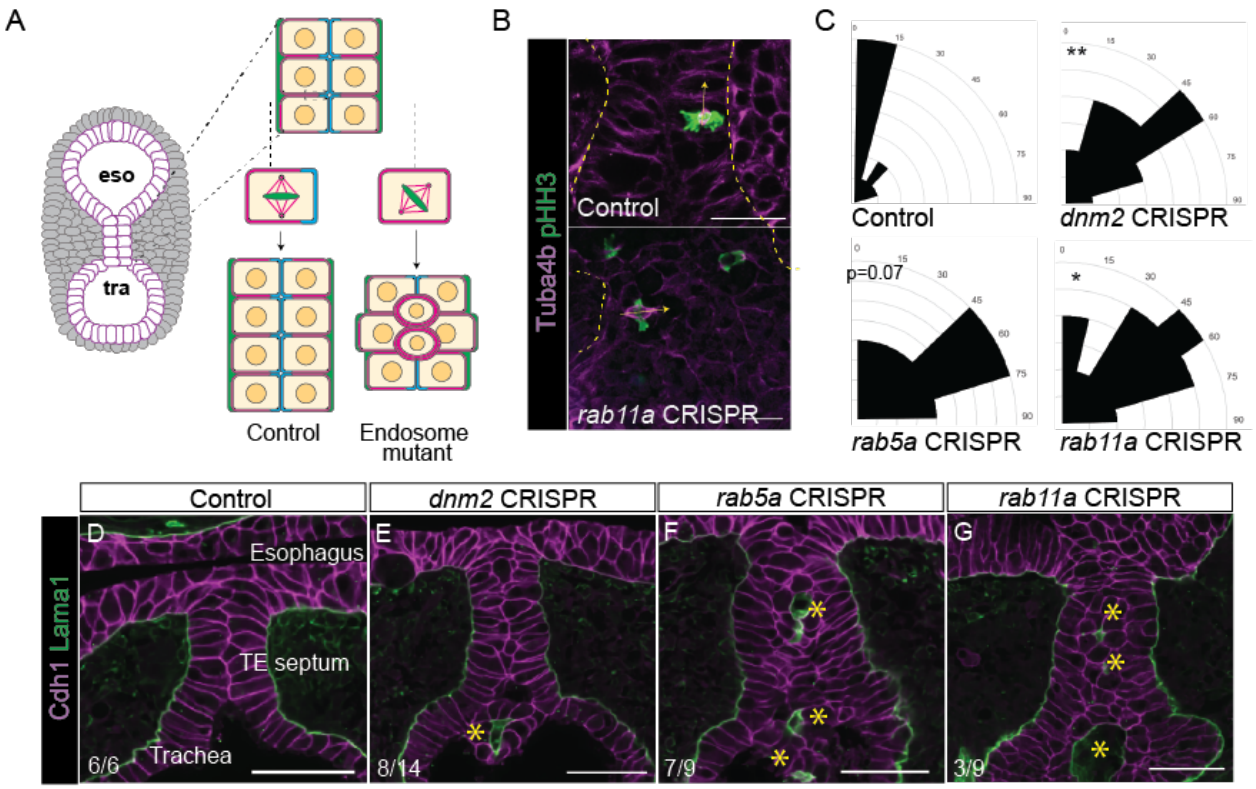

Figure 4. Endosome trafficking controls polarity of epithelial cell division. A) A potential model of altered cell division orientation in endosome mutants causes cells to accumulate in the epithelial septum. B) Immunostaining of the mitotic spindle (Tuba4a and phospho-H3 histone) was using to measure the angle of cell division. C) Distribution of mitotic spindle angles is random in endosome mutant epithelial cells compared to controls, which consistently divide between 0-15° (n=3-15 spindles per embryo, Fisher's exact test, *p<0.05, **p<0.01, N=4-6 embryos. D-G) Endosome mutants have ectopic Laminin deposits (asterisks) inside the blistered disorganized epithelial. Scale bars are 50 µm.

distribution of mitotic spindle angles (Figure 4B,C). This defect was localized to the septum, as the mitotic spindle angles in the trachea and esophagus were not significantly different between mutants and controls (Figure S4). Thus, loss of endosomal trafficking causes aberrant cell division into the center of the transient epithelial bilayer.

To test whether these changes in the orientation of cell division were linked to altered apical-basal cell polarity in the septum, we performed immunostaining for laminin, which is normally secreted from the basal side of epithelia into the extracellular matrix. We observed that mutant embryos exhibited ectopic laminin deposition in the center of the disorganized septum surrounding the round central cells and in the lumens of blisters within the tissue (Figure 4D-G). These observations are consistent with disrupted endosome trafficking leading to loss of apical-

basal polarity in the transient epithelial bilayer, randomized cell division, and cells accumulating in the mutant tracheoesophageal septum.

Endosome trafficking localizes Vangl2 to maintain apical memory in the epithelial bilayer

During tracheoesophageal morphogenesis, when the foregut epithelial cells from either side touch one another, they lose apical markers (aPKC, Par3) and upregulate Cdh1 (typically basal -lateral) as they adhere and form the transient bilayer. Despite this apparent loss of apical identity, the cells must somehow retain some apical-basal information to form an organized bilayer and undergo cell division in the plane of the epithelium – a process that we found requires endosome trafficking. One candidate pathway that might regulate this process is the Vangl-Celsr polarity complex. In addition to their well-known role in the Wnt/PCP pathway where heterotypic cell-cell interactions between transmembrane Vangl, Celsr, and Frizzled proteins govern cell orientation in the plane of the epithelia[23], Vangl and Celsr are also involved in specifying apical-basal polarity in epithelia by recruiting apical Par3 and aPKC whilst restricting Scrib to the basolateral domain [16,24,25]. Furthermore, apical Vangl-Celsr complexes are reported to be internalized by endosomes during polarized cell divisions of the fetal mouse epidermis [26], suggesting a potential mechanistic link in the foregut.

To assess whether Vangl2 and Celsr1 are involved in endosome-dependent epithelial remodeling in the foregut, we performed immunostaining in combination with Rab11a. Prior to foregut fusion, a low level of diffuse Vangl2 was observed throughout the foregut epithelia with no obvious difference between apical and basolateral cell domains (Figure 5A,F, Figure S5A), but as the midline epithelia touched, Vangl2 became progressively enriched and co-localized with Rab11a puncta at the apical contact point (Figure 5B,E,G). Once the transient bilayer formed, robust Rab11a-Vangl2 co-localization was observed at the adherent interface between the two epithelial (Figure 5C,E,H) but not at the luminal/apical cells surface of the dorsal esophagus or ventral trachea (Figure 5A-D, Figure S5B). This was somewhat unexpected since Vangl2 normally recruits apical Par and aPKC proteins. However, in this case, Rab11-Vangl2 co-localization is associated with a loss of apical markers and the accumulation of basal-lateral Cdh1. At NF41, Vangl2 and Rab11a levels at the cell membrane were downregulated as cells in the bilayer lose contact with one another (Figure 5D-E). In contrast to this dynamic Vangl2 subcellular localization, Celsr1 remained around the entire juxta-membrane region of the epithelial bilayer cells throughout tracheoesophageal morphogenesis, suggesting that it only complexes with Vangl2 as the midline epithelial cells come in contact. (Figure S5C-H).

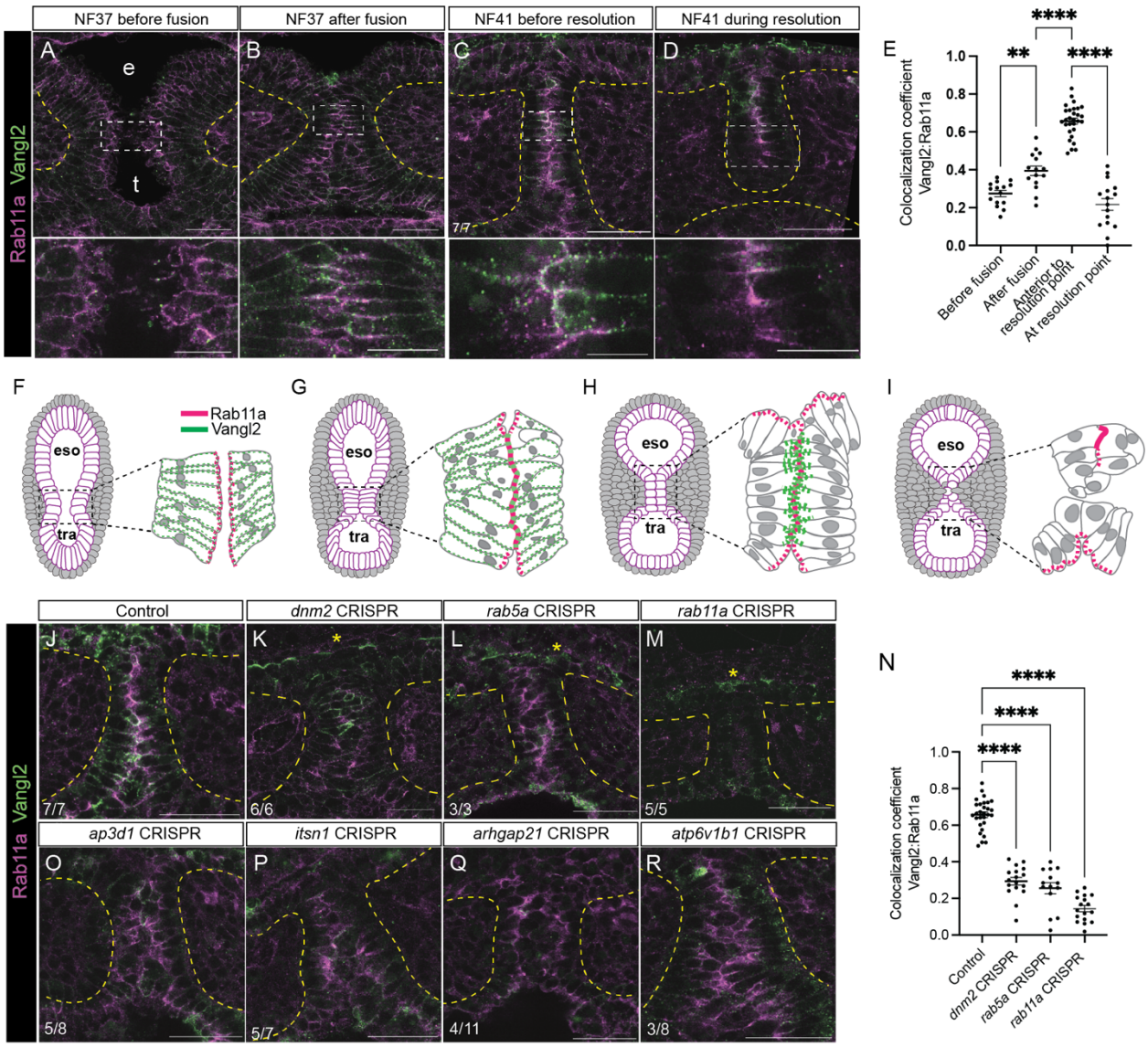

Figure 5. Rab11a recycling endosomes localize Vangl2 to maintain apical memory in the trachea-esophageal septum. A-D) Time course of Vangl2-Rab11a immunostaining during *Xenopus* tracheoesophageal separation. E) Dynamic Vangl2-Rab11a co-localization at the epithelial interface (Mean Pearson colocalization coefficient ± SEM, *** p<0.001, **** p<0.0001 1W-ANOVA, n=6 cells per embryo, N=5 embryos per stage). F-I) Diagrams depicting Vangl2-Rab11a localization during foregut separation. J-M) Vangl2 is mis-localized in septum epithelial cells of endosome mutants. N) Endosome mutant septa have significantly lower Vangl2-Rab11a colocalization relative to controls (mean ± SEM, **** p <0.0001 1W-ANOVA, n=5 cells per embryo, N=4-6 embryos per condition). O-R) CRISPR F0 mutation of patient variant orthologous genes in *Xenopus* (*ap3d1, itsn1, arhgap21*, and *atp6v1b1)* disrupts Vangl2-Rab11a co-localization in the TE septum. Scale bars are 50 µm (20µm in insets).

363 Considering that endosomes can internalize cell surface Vangl in the fetal mouse epidermis [26],
364 these data suggested that Vangl2 might be a cargo of the Rab11+ recycling endosomes,
365 transporting it to the cell surface where the epithelia fuse. To test this possibility, we examined
366 Vangl2 localization in the endosome mutants. Indeed Vangl2-Rab11a co-localization at the
367 epithelia contact was lost in the disorganized multilayer septum of *dnm2*, *rab5a* and *rab11a*
368 mutants (Figure 5J-N, Figure S5I). However, Celsr1 localization and apical Vangl2 in the
369 esophagus were unaffected (Figure 5K-M, asterisks, Figure S5J-N), indicating that recycling
370 endosomes are specifically required to localize Vangl2 in the fusing midline.
371
372 **Mutation of EA/TEF patient-like genes in *Xenopus* disrupted Rab11-Vangl2 localization**
373 We next assessed whether a similar mechanism could account for the TEF observed when we
374 mutated the *Xenopus* orthologs of endosome pathway risk genes from patients. These included
375 *AP3D1*, *ARHGAP21*, and *ITSN1* which encode adaptors and CDC42-GEFs respectively during
376 endocytic vesicle formation, as well as *ATP6V1B1*, which encodes a vacuolar ATPase subunit
377 required for acidification of endosomal vesicles [27-31]. As predicted, F0 CRISPR mutants of
378 *ap3d1*, *arhgap21*, *atp6v1b1* and *itsn1* all exhibited a loss of Vangl2-Rab11a co-localization and
379 a disorganized persistent septum (Figure 5O-R), consistent with these proteins functioning
380 upstream of Rab11 in the recycling endosome pathway.
381
382 Together these results indicate that during tracheoesophageal morphogenesis dynamic
383 recycling endosome activity is required to localize Vangl2 at the cell surface where the opposing
384 midline epithelia adhere to one another. Vangl2 appears to define an “apical memory” in the
385 epithelial bilayer cells which have lost aPKC and upregulate Cadherin, a membrane
386 configuration more typical of adherent basal-lateral cell-cell contacts. This unexpected behavior
387 is distinct from the typical roles for Vangl2 in apical-basal and planar cell polarity.
388
389 **Loss of Vangl or Celsr disrupts tracheoesophageal morphogenesis resulting in TEF**
390 The results above imply that Vangl-Celsr is required for tracheoesophageal morphogenesis.
391 Interestingly, one patient from our EA/TEF cohort had a heterozygous *de novo* damaging
392 missense variant in *CELSR2* predicted to alter an amino acid (asparagine to serine) in an N-
393 terminal cadherin domain [21,32]. Moreover, a search of clinical genetic databases and the
394 published literature revealed additional patients with sequence variants or copy-number
395 variation in *VANGL1*, *VANGL2*, *CELSR1*, and *CELSR2* who had EA/TEF or poorly defined

396 upper gastrointestinal and/or respiratory phenotypes all suggestive of structural foregut
397 anomalies (Table S2).
398
399 We therefore generated loss of function CRISPR-Cas9 F0 *Xenopus* mutants for *celsr2*, *celsr1,*
400 or *vangl2* with a 45-95% damaging indel rate, all of which exhibited a variably penetrant TEF
401 with a failure to separate the Sox2+ esophagus and Nkx2-1+ trachea at NF44 (Table S1).
402 Examination of the mutant foreguts at NF40, revealed a disorganized, thicker septum with round
403 cells in the middle and frequent blisters, phenocopying the endosome mutants (Figure 6A-H).
404 Moreover, the *celsr1 and celsr2* mutants exhibited a reduction in Vangl2 immunostaining,
405 consistent with previous reports that Celsr1 forms a heterotypic cell-cell complex with Vangl2[23].
406 Interestingly, in *vangl2* and *celsr1/2* mutants Rab11a was still localized to the contact surface in
407 middle the septum (Figure 6E-H), indicating that Vangl and Celsr are required for
408 tracheoesophageal morphogenesis downstream of recycling endosomes. Together our results
409 suggest that an unexpected but evolutionarily conserved endosome-cell polarity pathway
410 controls tracheoesophageal morphogenesis, and that disruptions to this process might
411 represent a previously unrecognized risk for EA/TEF in patients (Figure 6I).
412
413 **Discussion**
414 In this study we demonstrate that an endosome-cell polarity pathway is required for the
415 epithelial remodeling that drives *Xenopus* tracheoesophageal morphogenesis. We discovered
416 that Rab11+ recycling endosomes localize the transmembrane polarity protein Vangl2 to the
417 contact surface where foregut epithelia fuse. This appears to confer an “apical memory” which is
418 essential to maintain an organized transient epithelial bilayer and its subsequent fission into
419 distinct trachea and esophagus (Figure 6I). This unexpected Rab11-Vangl2 activity is distinct
420 from its typical roles in planar cell polarity and apical basal polarity and may represent a general
421 paradigm for epithelial fusion and fission during morphogenesis.
422
423 Previous studies in *Xenopus* gastrulation and neural tube morphogenesis have shown that
424 Vangl2 functions upstream of Rab11 in classical Wnt/PCP and apical-basal polarity roles to
425 regulate convergent extension and apical constriction. Vangl2 controls Rab11 localization for
426 apical constriction of gastrula bottle cells and in the neural plate hinge point. In addition, Vangl2-
427 mediated planar cell polarization is required for medial-apical localization of Rab11 in
428 convergent extension and the closing neural tube [33-35]. In the developing mouse pancreas,
429 apical restriction of Vangl2 maintains epithelial integrity and survival of progenitor cells through

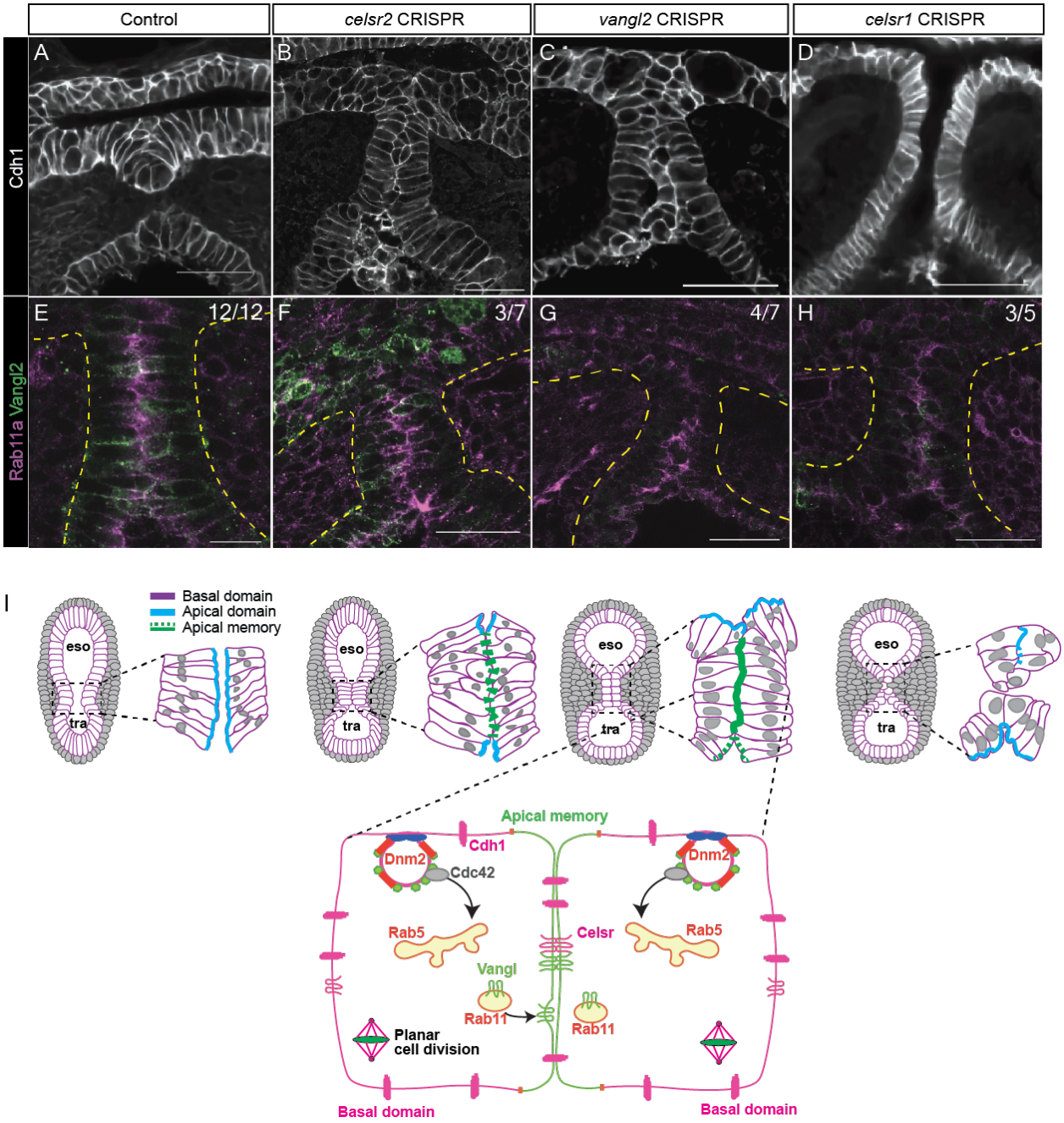

Fig. 6. Loss of Vangl or Celsr disrupts tracheoesophageal morphogenesis resulting in TEF. (A-D) Cdh1 immunostaining in shows that *celsr2*, *vangl2*, and *celsr1* mutants have TEF and (E-H) disorganized epithelial septa that fail to co-localize Vangl2-Rab11a. Scale bars are 50 µm. I) Model of how endosome trafficking of Vangl2 maintains apical-basal polarity information and the proper tissue organization required for tracheoesophageal morphogenesis.

439 modulating ROCK signaling activity, independent of apical-basal cell polarity[36]. Loss of
440 Rab11a/b in the pancreas leads to highly disorganized epithelial defects due to the mis-
441 localization of apical-basal proteins laminin, Par3, and aPKC, but this study did not examine
442 whether this was due to Vangl mis-localization [37]. Interestingly, Vangl2 has a PCP-independent
443 role in the developing lung mesenchyme during branching morphogenesis [38,39]. Neither the
444 *looptail* mutation nor conditional knockout of Vangl2 using ShhCre impairs trachea-esophageal
445 separation, however, a different Cre driver with earlier recombination in the foregut might lead to
446 separation anomalies. One example where Rab11 functions upstream of Vangl2, like we have
447 observed, is during mitosis of the mouse fetal epidermis, where endosomes internalize apical-
448 basal polarized Vangl, Celsr, and Fzd proteins which are later recycled back to the appropriate
449 cell surface after cell division [26]. A similar mechanism might explain the maintenance of
450 polarized cell division in the transient epithelial bilayer of the foregut, but in the mouse epidermis
451 this is a classical polarized epithelium, and in the foregut Vangl2 confers "apical memory" to
452 cells that have otherwise lost apical character. Another distinction between what we have
453 described in the foregut and these other examples of Vangl-regulated epithelial polarity in
454 morphogenesis is that in the foregut the epithelia first fuses (like the neural tube and palate) but
455 then undergo fission. Other tissues that experience this type of dynamic fusion-fission
456 morphogenesis include separation of anorectal tubes in the hindgut and semicircular canals in
457 the ear [40,41,42]. We predict that similar Rab11a-Vangl2 mechanisms may act in those tissues.
458
459 Our data, together with previously published work, suggests that Vangl2 is a cargo of Rab11a+
460 endosomes that transport newly synthesized Vangl2 from the ER-Golgi to the fusion surface, or
461 recycle Vangl2 from basolateral membranes. We postulate that other endosomal cargo may
462 include Cadherins and Integrins that facilitate tissue adhesion, and Laminins that mediate
463 interaction with the adjacent mesoderm at the basal surface. Consistent with this possibility we
464 note that EA/TEF patients were identified with potentially damaging variants in *ITGB4* and
465 *LAMB4* [21]. While initial Cdh1 (E-Cadherin) localization to the fusion surface was not affected by
466 disrupted endosome trafficking, the normal downregulation of Cdh1 at the fission step does not
467 occur in endosome or Vangl-Celsr mutants, which might explain why the foregut does not
468 separate properly. This suggests that endosomes may also be required to internalize cell
469 adhesion proteins during epithelial fission. One candidate pathway that might regulate
470 endosome-mediated loss of adhesion is the Eph/Ephrin pathway. Eph/Ephrin are known to
471 regulate tissue separation and cell sorting in many contexts[43] and *Efnb2* was recently shown to
472 be required for trachea-esophageal separation downstream of Nkx2-1[44,45]. We were not able to

473 assess Ephrin-Cadherin-endosome-Vangl interactions because effective Eph/Ephrin antibodies
474 are not currently available, however in the future it would be intriguing to generate transgenic
475 *Xenopus* or mice with tagged fusion proteins to test this possibility.
476
477 Endosome trafficking is a ubiquitous cell pathway required for homeostasis and many basic
478 cellular functions. Several pleiotropic diseases are associated with variants in endosome
479 trafficking genes [20], but interestingly many of these are rather specific to certain tissues. Not
480 surprisingly, total loss of endosome activity leads to early embryonic lethality in germline mutant
481 mice [46,47] and in *Xenopus* embryos results in gastrulation and neurulation defects [33]. Our F0
482 CRISPR mutagenesis on the other hand results in 30-90% damaging indels and therefore is
483 only a partial loss of function. Indeed, in our experiments endosome mutant embryos have a
484 significantly higher frequency of gastrulation and neurulation defects compared to controls
485 where the pigmentation gene *tyr* was mutated. In our experiments we selected those embryos
486 that survived to later stages. The fact that later embryos with partial loss of endosome activity
487 show specific defects suggests that some morphogenetic events like tracheoesophageal
488 separation represent developmental bottle necks that are particularly sensitive. This may
489 partially explain why EA/TEF patients frequently present with variants predicted to have partial
490 loss of function or hypomorphic variants in endosome and polarity pathway genes.
491
492 The EA/TEF risk genes that we validated in this study are predicted to function at various levels
493 of endosome trafficking pathways including formation of an endocytic vesicle (ITSN1, AP1G2),
494 cytoskeletal transport (ARHGAP21, ABRA, RASAL2, RAPGEF3), and endosomal acidification
495 (ATP6V1B1). We also discovered that a number of variants in CELSR1/2 and VANGL1/2,
496 including a damaging missense variant in CELSR2 in a patient from this cohort, are implicated
497 in EA/TEF and other foregut anomalies[21,48]. Furthermore, variants in VANGL1/2 underlie a
498 broad spectrum of developmental anomalies in humans[23] such as neural tube anomalies[49,50],
499 renal anomalies [51,52], congenital heart anomalies[53,54], and lung diseases[55], and may be trafficked
500 by endosomes to specific cellular domains during development of these organs. Complex
501 EA/TEF patents tend to have comorbidities in these same organs that experience tissue fusion
502 events during fetal development[21]. This suggests that disruption of a conserved endosome-
503 polarity pathway may account for pleiotropic phenotypes in many complex EA/TEF patients.
504 Together this suggests the provocative possibility of an endosomeopathy developmental
505 syndrome, akin to ciliopathies. Further comparative analysis of patient genetics and animal
506 models will improve our understanding of fundamental tissue fusion and fission events in

507 development and advance our knowledge of the developmental basis of congenital anomalies,
508 informing the care and treatment of endosomeopathy patients.
509

510 **Acknowledgements**
511 We thank the Bio-Imaging and Analysis Facility and Dr. Matthew Kofron for imaging and
512 analysis advice (RRID:SCR_022628), the Division of Veterinary Services, and the DNA
513 Sequencing Core at CCHMC (RRID:SCR_022630) for their services used in this study. We
514 thank S. Sokol for kindly providing the anti-Vangl2 antibody. We thank the members of the
515 CLEARconsortium.org for access to EA/TEF patient data and for helpful discussions. This work
516 is supported by NICHD P01HD093393 to YS, WKC, and AMZ, and a Canadian Institutes of
517 Health Research postdoctoral fellowship to NAE.
518

519 **Author contributions**
520 Conceptualization: NAE, AMZ. Formal analysis: NAE, AK, AMZ. Funding acquisition: YS, WKC,
521 AMZ. Investigation: NAE, AK, AW, ZA, APK. Methodology: NAE. Project administration: NAE,
522 AMZ. Supervision: NAE, AMZ. Validation: NAE. Visualization: NAE, AMZ. Writing – original
523 draft: NAE, AMZ. Writing – review & editing: all authors.
524

525 **Declaration of interests**
526 The authors declare no competing interests.
527

528 **Methods**
529 **Experimental models**
530 *Xenopus* experiments were performed using Cincinnati Children's Hospital Medical Center
531 (CCHMC) Institutional Animal Care and Use Committee (IACUC 2022-0026) approved
532 guidelines. Adult *Xenopus tropicalis* and *Xenopus laevis* frogs were purchased from NASCO
533 and Xenopus1 (USA) and housed in the CCHMC vivarium under standard housing conditions.
534 *Xenopus* embryos were obtained by *in vitro* fertilization according to standard procedures [56].
535 *Sox2* germline mutant embryos were generated at the National *Xenopus* Resource according to
536 standard procedures (RRID:SCR_013731).
537

538 **CRISPR-Cas9 gene editing and Xenopus embryo culture**
539 Guide RNAs and genotyping primers were designed using CRISPRScan, InDelphi, and
540 CRISPOR predictive algorithms [57] and synthesized as altR-cRNA by IDT (sequences in

541 Resources Table and Table S3). After annealing with tracrRNA to create a single gRNA, gRNAs
542 were combined with recombinant Cas9 protein (PNA Biosciences) and injected into 1-2 cell
543 stage *Xenopus* embryos at a final concentration of 500-700pg gRNA and 1-1.5ng Cas9p.
544 *Xenopus tropicalis* embryos were raised at 25°C in 0.1X Modified Barth's solution (MBS) for
545 three days post fertilization before being anesthetized and fixed at NF44 in MEMFA (3.7%
546 formaldehyde, 0.1M MOPS, 2mM EGTA, 1mM $MgSO_4$) for 1hr at room temperature, then in
547 Dent's solution (80% methanol, 20% DMSO) for long term storage at -20°C. *Xenopus laevis*
548 embryos were raised between 15-21°C in 0.1X MBS for 3-5 days post fertilization (to stages
549 NF37-44), then anesthetized and fixed in MEMFA or 2% trichloroacetic acid (for endosome
550 proteins and Vangl2 immunostaining) for 30-40 mins at room temperature. Embryos were
551 immunostained and imaged by confocal microscopy as outlined in the next section prior to
552 genotyping. Genotyping for CRISPR-Cas9 editing efficiency was performed as described in
553 Zhong et al., 2022[21] using the primer sequences in Resources Table and Table S3. Percent
554 indel efficiency was determined by Sanger sequencing of PCR products and quantified using
555 Inference of CRISPR Edits (Synthego, USA). A minimum of 20 individual mutant embryos from
556 3 independent editing experiments were analyzed to identify a statistically significant frequency
557 of trachea-esophageal anomalies by Student's t-test from the 2% baseline detected in controls.
558

559 **Whole mount immunostaining and confocal microscopy**

560 Whole mount immunostaining on *Xenopus* tissue was performed as described in Nasr et al.,
561 2019[13] and Zhong et al., 2022[21] with the following modifications for imaging endosome and
562 polarity proteins: fixed embryos were rehydrated in PBS, embedded in 2% low melt agarose in
563 PBS, and sectioned with a Vibratome VT1000S (Leica) to obtain 200 µm tissue slices containing
564 the trachea and esophagus. Slices were permeabilized with 0.1% Triton X-100 in PBS (0.3%
565 Triton X-100 for anti-Vangl2), blocked in 5% normal donkey serum in PBS, then incubated in
566 primary antibody (1:100) in blocking solution overnight at 4°C. Slices were incubated in Alexa
567 fluor-conjugated secondary antibody (1:500) in blocking solution for 2 hours at room
568 temperature, then dehydrated in 100% methanol. For confocal microscopy, slices were cleared
569 in BABB and imaged on a Nikon A1 inverted laser scanning confocal microscope with a 10X,
570 20X water immersion, or 40X oil immersion objective (Nikon USA).
571

572 **Image analyses**

573 *Signal intensity quantification*: Signal intensity quantification was performed in ImageJ (NIH).
574 Regions of interest (ROI) were drawn around the apical and basal membranes, then mean gray

575 value was measured and plotted as mean intensity ± max/min. At least five cells were measured
576 per embryo in a minimum of five embryos per condition for quantification and statistical analysis
577 by 2W-ANOVA.
578
579 *Prolate ellipticity and surface contact area*: Prolate ellipticity and surface contact area
580 measurements were performed in Imaris (Bitplane). 3D cell volumes were rendered based on E-
581 Cadherin staining and surface models were generated. Prolate ellipticity was measured from
582 rendered surfaces of epithelial cells and plotted as mean ± max/min. Values approaching 1
583 have elongated shapes while values approaching 0 have spherical shapes. Surface-surface
584 contact area between the esophagus and trachea-esophageal septum, within the trachea-
585 esophageal septum, and between the trachea and trachea-esophageal septum was measured
586 from rendered surfaces of epithelial cells using the Surface-Surface Contact Area XTension and
587 plotted as the mean ± max/min. At least five cells were measured per embryo in a minimum of
588 five embryos per condition for quantification and statistical analysis by unpaired Student's t-test
589 (prolate ellipticity) and 1W-ANOVA (surface contact area).
590
591 *Three-dimensional measurements of axes in the foregut*: Three dimensional lengths of x
592 (medial), y (dorsal-ventral), and z (rostral-caudal) axes were performed in Imaris (Bitplane). 3D
593 cell volumes were rendered based on E-Cadherin staining and surface models were generated.
594 Lengths were measured from rendered surfaces of epithelial cells and plotted as the mean
595 length of each axis ± standard error of the mean. At least five embryos were measured for
596 quantification and statistical analysis by unpaired Student's t-test.
597
598 *Mitotic spindle orientation*: Mitotic spindle orientation angles were obtained in ImageJ (NIH) as
599 described in Franco and Carmena, 2019[58]. Only images with z-sections through the axial axis of
600 *Xenopus* embryos containing clearly identifiable mitotic spindles stained with anti-α-tubulin were
601 analyzed for spindle angles. One line of the angle was drawn through linking both centrosomes,
602 and the second line of the angle was drawn parallel to the basement membrane of the epithelial
603 cell. Measurements were collected and wind rose plots were generated in Excel. At least three
604 mitotic spindles were measured in a minimum of 5 embryos for quantification and statistical
605 analysis by Fisher's exact test.
606
607 *Colocalization*: Pearson colocalization coefficients between Vangl2/Rab11a, Cdh1/Rab11a, and
608 Celsr1/Rab11a immunostaining signals were calculated in Nikon Elements (Nikon USA). ROIs

609 were drawn around an entire cell, and the Pearson colocalization coefficient was determined. A
610 coefficient of 1 indicates two channels whose fluorescence intensities are perfectly linearly
611 related. At least six cells were measured in a minimum of 5 embryos for quantification and
612 statistical analyses by 1W-ANOVA.
613
614 **Immunoblotting**
615 Whole Xenopus embryos or microdissected anterior foregut tissue (from pharynx to stomach)
616 were pooled and lysed in Triton X-100 lysis buffer (0.5% Triton X-100, 0.1M HEPES, 150 mM
617 NaCl, 2mM EDTA pH 8.0, 2mM EGTA) containing protease inhibitors (ThermoFisher). Protein
618 lysates were combined with 2X Laemmli buffer and 0.1M DTT, boiled, and separated by 4-12%
619 Bis-Tris gel electrophoresis (ThermoFisher). For HRP detection, membranes were blocked in
620 5% BSA, then incubated in primary antibody (1:1000) overnight in blocking solution at 4°C.
621 Membranes were incubated in HRP-conjugated secondary antibody (1:5000) in blocking
622 solution for 1 hour at room temperature, then visualized by addition of ECL substrate
623 (Amersham, GE) and imaged using a ChemiDoc (BioRad). Western blot quantification was
624 performed in ImageLab (BioRad). For fluorescence-based detection, membranes were blocked
625 in Odyssey blocking buffer (LI-COR), then incubated in primary antibody (1:1000) overnight in
626 blocking buffer at 4°C. Membranes were incubated in IRDye-conjugated secondary antibodies
627 (1:5000) in blocking buffer for 1 hour at room temperature, then visualized using an Odyssey
628 Dlx Imager (LI-COR). Quantification was performed with LI-COR Acquisition software.
629
630 **Clinical genetic database mining**
631 Deidentified case data for variants in CELSR1/2 and VANGL1/2 were searched in NCBI
632 PubMed and the DECIPHER database (https://www.deciphergenomics.org). Results from the
633 DECIPHER database were filtered for EA/TEF related phenotypes including “Feeding difficulties
634 in infancy”, “Abnormal esophagus morphology”, “Respiratory distress”, “Laryngeal stenosis”,
635 and “Respiratory insufficiency”.
636
637 **Resources**
638

Antibodies		
Rabbit anti-PKC zeta	Abcam	ab59364; RRID:AB_944858
Mouse anti-Cdh1	Developmental Studies Hybridoma Bank	5D3 (deposited to the DSHB by Gumbiner, B.M.); RRID:AB_528116

Rabbit anti-Dnm2	Abcam	Ab65556; RRID:AB_1603781
Rabbit anti-Rab5a	Cell Signaling Technology	3547; RRID:AB_2300649
Rabbit anti-Rab11a	Thermo Fisher Scientific	700184; RRID:AB_2532295
Mouse anti-Rab11a	BD Biosciences	610657; RRID:AB_397984
Rabbit anti-Tjp1 (ZO-1)	Thermo Fisher Scientific	61-7300; RRID:AB_138452
Rabbit anti-Par3	Millipore	07-330; RRID:AB_2101325
Mouse anti-Tuba4b	Sigma	T9026; RRID:AB_477593
Rabbit anti-Lama1	Sigma	L9393; RRID:AB_477163
Rabbit anti-pHH3 (Ser10)	Cell Signaling Technology	9701; RRID:AB_331535
Rabbit anti-Vangl2	S. Sokol lab	RRID:AB_2744499
Rabbit anti-Celsr1	BiCell Scientific	50801
Mouse anti-Sox2	Abcam	ab79351; RRID:AB_10710406
Rabbit anti-Nkx2-1	Santa Cruz	sc-13040; RRID:AB_793532
Goat anti-Foxf1	R&D Systems	AF4798; RRID:AB_2105588
Rabbit anti-Itsn1	Millipore	ABS984
Chemicals		
Cas9 protein	PNA Biosciences	CP01-50
Experimental models: organisms/strains		
Xenopus laevis females	NASCO	LM00531
Xenopus laevis males	NASCO	LM00715
Xenopus tropicalis females	Xenopus1	
Xenopus tropicalis males	Xenopus1	
Xenopus tropicalis sox2 mutant embryos	National Xenopus Resource	NXR_3051; Xtr.sox2^{tmHorb}
Oligonucleotides *(See also Table S3)*		
Rab11a.S gRNA GAGATTACTCTTCCCCACAC	IDT	Nasr et al., 2019[13]
Rab5a gRNA CGACTGCAGATTCTCCTAAA	IDT	This study
Dnm2 gRNA CGGAGACCGAGTGCAGCCAT	IDT	This study
Slc45a2 gRNA GGTTACATAGGCTGCCTCCA	IDT	Delay et al., 2018[59]
Genotyping, Rab11a.S forward primer ACAGTGTGCATAGAATTTGGCG	IDT	This study
Genotyping, Rab11a.S reverse primer CGTGTGTTGCCTAGAGGGAC	IDT	This study
Genotyping, Dnm2.S forward primer GGAGCCAGCGAGAAACACTTA	IDT	This study
Genotyping, Dnm2.S reverse primer GCGACAATATCAACCCACCAA	IDT	This study
Genotyping, Dnm2.L forward primer	IDT	This study

AGGGAAACACTTACCGGCCTA		
Genotyping, Dnm2.L reverse primer GAAACACAACCAATCACAATCCCT	IDT	This study
Genotyping, Rab5a.S forward primer ACCCTGGCAAACTTTGTGGT	IDT	This study
Genotyping, Rab5a.L forward primer GAGCATCCAACCCACCCTTT		This study
Genotyping, Rab5a reverse primer ACTGTCCCTTTACGAAGCGA	IDT	This study
Software		
NIS Elements	Nikon	RRID:SCR_014329
ImageJ	NIH	RRID:SCR_003070
IMARIS	Oxford Instruments	RRID:SCR_007370
Surface-Surface Contact Area XTension	Oxford Instruments	https://imaris.oxinst.com/open/view/surface-surface-contact-area
Prism 9	GraphPad	RRID:SCR_002798
Inference of CRISPR edits (ICE)	Synthego	http://www.ice.synthego.com
ImageLab	BioRad	RRID:SCR_014210

References

1. Edwards, N.A., Shacham-Silverberg, V., Weitz, L., Kingma, P.S., Shen, Y., Wells, J.M., Chung, W.K., and Zorn, A.M. (2021). Developmental basis of trachea-esophageal birth defects. Dev Biol *477*, 85-97. 10.1016/j.ydbio.2021.05.015.

2. Raad, S., David, A., Que, J., and Faure, C. (2020). Genetic Mouse Models and Induced Pluripotent Stem Cells for Studying Tracheal-Esophageal Separation and Esophageal Development. Stem Cells Dev *29*, 953-966. 10.1089/scd.2020.0075.

3. van Lennep, M., Singendonk, M.M.J., Dall'Oglio, L., Gottrand, F., Krishnan, U., Terheggen-Lagro, S.W.J., Omari, T.I., Benninga, M.A., and van Wijk, M.P. (2019). Oesophageal atresia. Nat Rev Dis Primers *5*, 26. 10.1038/s41572-019-0077-0.

4. Chitkara, A.E., Tadros, M., Kim, H.J., and Harley, E.H. (2003). Complete laryngotracheoesophageal cleft: complicated management issues. Laryngoscope *113*, 1314-1320. 10.1097/00005537-200308000-00010.

5. Bednarczyk, D., Sasiadek, M.M., and Smigiel, R. (2013). Chromosome aberrations and gene mutations in patients with esophageal atresia. J Pediatr Gastroenterol Nutr *57*, 688-693. 10.1097/MPG.0b013e3182a373dc.

656 6. Stoll, C., Alembik, Y., Dott, B., and Roth, M.P. (2017). Associated anomalies in cases with
657 esophageal atresia. Am J Med Genet A *173*, 2139-2157. 10.1002/ajmg.a.38303.

658 7. Brosens, E., Ploeg, M., van Bever, Y., Koopmans, A.E., H, I.J., Rottier, R.J., Wijnen, R., Tibboel,
659 D., and de Klein, A. (2014). Clinical and etiological heterogeneity in patients with tracheo-
660 esophageal malformations and associated anomalies. Eur J Med Genet *57*, 440-452.
661 10.1016/j.ejmg.2014.05.009.

662 8. Li, Y., Litingtung, Y., Ten Dijke, P., and Chiang, C. (2007). Aberrant Bmp signaling and notochord
663 delamination in the pathogenesis of esophageal atresia. Dev Dyn *236*, 746-754.
664 10.1002/dvdy.21075.

665 9. Goss, A.M., Tian, Y., Tsukiyama, T., Cohen, E.D., Zhou, D., Lu, M.M., Yamaguchi, T.P., and
666 Morrisey, E.E. (2009). Wnt2/2b and beta-catenin signaling are necessary and sufficient to specify
667 lung progenitors in the foregut. Dev Cell *17*, 290-298. 10.1016/j.devcel.2009.06.005.

668 10. Harris-Johnson, K.S., Domyan, E.T., Vezina, C.M., and Sun, X. (2009). beta-Catenin promotes
669 respiratory progenitor identity in mouse foregut. Proc Natl Acad Sci U S A *106*, 16287-16292.
670 10.1073/pnas.0902274106.

671 11. Rankin, S.A., Han, L., McCracken, K.W., Kenny, A.P., Anglin, C.T., Grigg, E.A., Crawford, C.M.,
672 Wells, J.M., Shannon, J.M., and Zorn, A.M. (2016). A Retinoic Acid-Hedgehog Cascade
673 Coordinates Mesoderm-Inducing Signals and Endoderm Competence during Lung Specification.
674 Cell Rep *16*, 66-78. 10.1016/j.celrep.2016.05.060.

675 12. Kim, E., Jiang, M., Huang, H., Zhang, Y., Tjota, N., Gao, X., Robert, J., Gilmore, N., Gan, L., and
676 Que, J. (2019). Isl1 Regulation of Nkx2.1 in the Early Foregut Epithelium Is Required for Trachea-
677 Esophageal Separation and Lung Lobation. Dev Cell *51*, 675-683 e674.
678 10.1016/j.devcel.2019.11.002.

679 13. Nasr, T., Mancini, P., Rankin, S.A., Edwards, N.A., Agricola, Z.N., Kenny, A.P., Kinney, J.L.,
680 Daniels, K., Vardanyan, J., Han, L., et al. (2019). Endosome-Mediated Epithelial Remodeling
681 Downstream of Hedgehog-Gli Is Required for Tracheoesophageal Separation. Dev Cell *51*, 665-
682 674 e666. 10.1016/j.devcel.2019.11.003.

683 14. Cote, L.E., and Feldman, J.L. (2022). Won't You be My Neighbor: How Epithelial Cells Connect
684 Together to Build Global Tissue Polarity. Front Cell Dev Biol *10*, 887107.
685 10.3389/fcell.2022.887107.

686 15. Pickett, M.A., Naturale, V.F., and Feldman, J.L. (2019). A Polarizing Issue: Diversity in the
687 Mechanisms Underlying Apico-Basolateral Polarization In Vivo. Annu Rev Cell Dev Biol *35*, 285-
688 308. 10.1146/annurev-cellbio-100818-125134.

689 16. Aigouy, B., and Le Bivic, A. (2016). The PCP pathway regulates Baz planar distribution in
690 epithelial cells. Sci Rep *6*, 33420. 10.1038/srep33420.

691 17. Murdoch, J.N., Doudney, K., Paternotte, C., Copp, A.J., and Stanier, P. (2001). Severe neural
692 tube defects in the loop-tail mouse result from mutation of Lpp1, a novel gene involved in floor
693 plate specification. Hum Mol Genet *10*, 2593-2601. 10.1093/hmg/10.22.2593.

694 18. Butler, M.T., and Wallingford, J.B. (2018). Spatial and temporal analysis of PCP protein dynamics
695 during neural tube closure. Elife *7*. 10.7554/eLife.36456.

696 19. Torban, E., Wang, H.J., Patenaude, A.M., Riccomagno, M., Daniels, E., Epstein, D., and Gros, P.
697 (2007). Tissue, cellular and sub-cellular localization of the Vangl2 protein during embryonic
698 development: effect of the Lp mutation. Gene Expr Patterns *7*, 346-354.
699 10.1016/j.modgep.2006.07.007.

700 20. Yarwood, R., Hellicar, J., Woodman, P.G., and Lowe, M. (2020). Membrane trafficking in health
701 and disease. Dis Model Mech *13*. 10.1242/dmm.043448.

702 21. Zhong, G., Ahimaz, P., Edwards, N.A., Hagen, J.J., Faure, C., Lu, Q., Kingma, P., Middlesworth,
703 W., Khlevner, J., El Fiky, M., et al. (2022). Identification and validation of candidate risk genes in
704 endocytic vesicular trafficking associated with esophageal atresia and tracheoesophageal
705 fistulas. HGG Adv *3*, 100107. 10.1016/j.xhgg.2022.100107.

706 22. Szklarczyk, D., Kirsch, R., Koutrouli, M., Nastou, K., Mehryary, F., Hachilif, R., Gable, A.L., Fang,
707 T., Doncheva, N.T., Pyysalo, S., et al. (2023). The STRING database in 2023: protein-protein
708 association networks and functional enrichment analyses for any sequenced genome of interest.
709 Nucleic Acids Res *51*, D638-D646. 10.1093/nar/gkac1000.

710 23. Butler, M.T., and Wallingford, J.B. (2017). Planar cell polarity in development and disease. Nat
711 Rev Mol Cell Biol *18*, 375-388. 10.1038/nrm.2017.11.

712 24. Panzica, D.A., Findlay, A.S., van Ladesteijn, R., and Collinson, J.M. (2019). The core planar cell
713 polarity gene, Vangl2, maintains apical-basal organisation of the corneal epithelium. J Anat *234*,
714 106-119. 10.1111/joa.12676.

715 25. vandenBerg, A.L., and Sassoon, D.A. (2009). Non-canonical Wnt signaling regulates cell polarity
716 in female reproductive tract development via van gogh-like 2. Development *136*, 1559-1570.
717 10.1242/dev.034066.

718 26. Devenport, D., Oristian, D., Heller, E., and Fuchs, E. (2011). Mitotic internalization of planar cell
719 polarity proteins preserves tissue polarity. Nat Cell Biol *13*, 893-902. 10.1038/ncb2284.

720 27. Yang, Q., Li, G., Singh, S.K., Alexander, E.A., and Schwartz, J.H. (2006). Vacuolar H+ -ATPase
721 B1 subunit mutations that cause inherited distal renal tubular acidosis affect proton pump
722 assembly and trafficking in inner medullary collecting duct cells. J Am Soc Nephrol *17*, 1858-
723 1866. 10.1681/ASN.2005121277.

724 28. Dong, X., Li, H., Derdowski, A., Ding, L., Burnett, A., Chen, X., Peters, T.R., Dermody, T.S.,
725 Woodruff, E., Wang, J.J., and Spearman, P. (2005). AP-3 directs the intracellular trafficking of
726 HIV-1 Gag and plays a key role in particle assembly. Cell *120*, 663-674.
727 10.1016/j.cell.2004.12.023.

728 29. Kantheti, P., Qiao, X., Diaz, M.E., Peden, A.A., Meyer, G.E., Carskadon, S.L., Kapfhamer, D.,
729 Sufalko, D., Robinson, M.S., Noebels, J.L., and Burmeister, M. (1998). Mutation in AP-3 delta in
730 the mocha mouse links endosomal transport to storage deficiency in platelets, melanosomes, and
731 synaptic vesicles. Neuron *21*, 111-122. 10.1016/s0896-6273(00)80519-x.

732 30. Dubois, T., Paléotti, O., Mironov, A.A., Fraisier, V., Stradal, T.E., De Matteis, M.A., Franco, M.,
733 and Chavrier, P. (2005). Golgi-localized GAP for Cdc42 functions downstream of ARF1 to control
734 Arp2/3 complex and F-actin dynamics. Nat Cell Biol *7*, 353-364. 10.1038/ncb1244.

735 31. Gryaznova, T., Gubar, O., Burdyniuk, M., Kropyvko, S., and Rynditch, A. (2018). WIP/ITSN1
736 complex is involved in cellular vesicle trafficking and formation of filopodia-like protrusions. Gene
737 *674*, 49-56. 10.1016/j.gene.2018.06.078.

738 32. Wang, J., Ahimaz, P.R., Hashemifar, S., Khlevner, J., Picoraro, J.A., Middlesworth, W., Elfiky,
739 M.M., Que, J., Shen, Y., and Chung, W.K. (2021). Novel candidate genes in esophageal
740 atresia/tracheoesophageal fistula identified by exome sequencing. Eur J Hum Genet *29*, 122-130.
741 10.1038/s41431-020-0680-2.

742 33. Lee, J.Y., and Harland, R.M. (2010). Endocytosis is required for efficient apical constriction during
743 Xenopus gastrulation. Curr Biol *20*, 253-258. 10.1016/j.cub.2009.12.021.

744 34. Ossipova, O., Kim, K., Lake, B.B., Itoh, K., Ioannou, A., and Sokol, S.Y. (2014). Role of Rab11 in
745 planar cell polarity and apical constriction during vertebrate neural tube closure. Nat Commun *5*,
746 3734. 10.1038/ncomms4734.

747 35. Ossipova, O., Chuykin, I., Chu, C.W., and Sokol, S.Y. (2015). Vangl2 cooperates with Rab11 and
748 Myosin V to regulate apical constriction during vertebrate gastrulation. Development *142*, 99-107.
749 10.1242/dev.111161.

750 36. Flasse, L., Yennek, S., Cortijo, C., Barandiaran, I.S., Kraus, M.R., and Grapin-Botton, A. (2020).
751 Apical Restriction of the Planar Cell Polarity Component VANGL in Pancreatic Ducts Is Required
752 to Maintain Epithelial Integrity. Cell Rep *31*, 107677. 10.1016/j.celrep.2020.107677.

753 37. Barlow, H.R., Ahuja, N., Bierschenk, T., Htike, Y., Fassetta, L., Azizoglu, D.B., Flores, J., Gao, N.,
754 De la, O.S., Sneddon, J.B., et al. (2023). Rab11 is essential to pancreas morphogenesis, lumen
755 formation and endocrine mass. Dev Biol *499*, 59-74. 10.1016/j.ydbio.2023.05.002.

756 38. Paramore, S.V., Trenado-Yuste, C., Sharan, R., Devenport, D., and Nelson, C.M. (2022). Vangl
757 facilitates mesenchymal thinning during lung sacculation independently of Celsr. bioRxiv.
758 10.1101/2022.12.28.522148.

759 39. Paramore, S.V., Goodwin, K., Devenport, D., and Nelson, C.M. (2023). Mesenchymal
760 Vangl facilitates airway elongation and widening independently of the planar cell
761 polarity complex. bioRxiv, 2023.2007.2003.547543. 10.1101/2023.07.03.547543.

762 40. Seifert, A.W., Harfe, B.D., and Cohn, M.J. (2008). Cell lineage analysis demonstrates an
763 endodermal origin of the distal urethra and perineum. Dev Biol *318*, 143-152.
764 10.1016/j.ydbio.2008.03.017.

765 41. Martin, P., and Swanson, G.J. (1993). Descriptive and experimental analysis of the epithelial
766 remodellings that control semicircular canal formation in the developing mouse inner ear. Dev
767 Biol *159*, 549-558. 10.1006/dbio.1993.1263.

768 42. Alsina, B., and Whitfield, T.T. (2017). Sculpting the labyrinth: Morphogenesis of the developing
769 inner ear. Semin Cell Dev Biol *65*, 47-59. 10.1016/j.semcdb.2016.09.015.

770 43. Niethamer, T.K., and Bush, J.O. (2019). Getting direction(s): The Eph/ephrin signaling system in
771 cell positioning. Dev Biol *447*, 42-57. 10.1016/j.ydbio.2018.01.012.

772 44. Lewis, A.E., Kuwahara, A., Franzosi, J., and Bush, J.O. (2022). Tracheal separation is driven by
773 NKX2-1-mediated repression of Efnb2 and regulation of endodermal cell sorting. Cell Rep *38*,
774 110510. 10.1016/j.celrep.2022.110510.

775 45. Lewis, A.E., Hwa, J., Wang, R., Soriano, P., and Bush, J.O. (2015). Neural crest defects in
776 ephrin-B2 mutant mice are non-autonomous and originate from defects in the vasculature. Dev
777 Biol *406*, 186-195. 10.1016/j.ydbio.2015.08.021.

778 46. Yu, S., Yehia, G., Wang, J., Stypulkowski, E., Sakamori, R., Jiang, P., Hernandez-Enriquez, B.,
779 Tran, T.S., Bonder, E.M., Guo, W., and Gao, N. (2014). Global ablation of the mouse Rab11a
780 gene impairs early embryogenesis and matrix metalloproteinase secretion. J Biol Chem *289*,
781 32030-32043. 10.1074/jbc.M113.538223.

782 47. Ferguson, S.M., Raimondi, A., Paradise, S., Shen, H., Mesaki, K., Ferguson, A., Destaing, O.,
783 Ko, G., Takasaki, J., Cremona, O., et al. (2009). Coordinated actions of actin and BAR proteins
784 upstream of dynamin at endocytic clathrin-coated pits. Dev Cell *17*, 811-822.
785 10.1016/j.devcel.2009.11.005.

786 48. Zhang, R., Gehlen, J., Kawalia, A., Melissari, M.T., Dakal, T.C., Menon, A.M., Hofele, J.,
787 Riedhammer, K., Waffenschmidt, L., Fabian, J., et al. (2020). Human exome and mouse
788 embryonic expression data implicate ZFHX3, TRPS1, and CHD7 in human esophageal atresia.
789 PLoS One *15*, e0234246. 10.1371/journal.pone.0234246.

790 49. Iliescu, A., Gravel, M., Horth, C., and Gros, P. (2014). Independent mutations at Arg181 and
791 Arg274 of Vangl proteins that are associated with neural tube defects in humans decrease protein
792 stability and impair membrane targeting. Biochemistry *53*, 5356-5364. 10.1021/bi500400g.

793 50. Merello, E., Mascelli, S., Raso, A., Piatelli, G., Consales, A., Cama, A., Kibar, Z., Capra, V., and
794 Marco, P.D. (2015). Expanding the mutational spectrum associated to neural tube defects:
795 literature revision and description of novel VANGL1 mutations. Birth Defects Res A Clin Mol
796 Teratol *103*, 51-61. 10.1002/bdra.23305.

797 51. Papakrivopoulou, E., Vasilopoulou, E., Lindenmeyer, M.T., Pacheco, S., Brzoska, H.L., Price,
798 K.L., Kolatsi-Joannou, M., White, K.E., Henderson, D.J., Dean, C.H., et al. (2018). Vangl2, a
799 planar cell polarity molecule, is implicated in irreversible and reversible kidney glomerular injury. J
800 Pathol *246*, 485-496. 10.1002/path.5158.

801 52. Schnell, U., and Carroll, T.J. (2016). Planar cell polarity of the kidney. Exp Cell Res *343*, 258-266.
802 10.1016/j.yexcr.2014.11.003.

803 53. Yuan, Y., Gao, Y., Wang, H., Ma, X., Ma, D., and Huang, G. (2014). Promoter methylation and
804 expression of the VANGL2 gene in the myocardium of pediatric patients with tetralogy of fallot.
805 Birth Defects Res A Clin Mol Teratol *100*, 973-984. 10.1002/bdra.23291.

806 54. Li, D., and Wang, J. (2018). Planar Cell Polarity Signaling in Mammalian Cardiac Morphogenesis.
807 Pediatr Cardiol *39*, 1052-1062. 10.1007/s00246-018-1860-5.

808 55. Yates, L.L., and Dean, C.H. (2011). Planar polarity: A new player in both lung development and
809 disease. Organogenesis *7*, 209-216. 10.4161/org.7.3.18462.

810 56. Wlizla, M., McNamara, S., and Horb, M.E. (2018). Generation and Care of Xenopus laevis and
811 Xenopus tropicalis Embryos. Methods Mol Biol *1865*, 19-32. 10.1007/978-1-4939-8784-9_2.

812 57. Naert, T., Tulkens, D., Edwards, N.A., Carron, M., Shaidani, N.I., Wlizla, M., Boel, A., Demuynck,
813 S., Horb, M.E., Coucke, P., et al. (2020). Maximizing CRISPR/Cas9 phenotype penetrance
814 applying predictive modeling of editing outcomes in Xenopus and zebrafish embryos. Sci Rep *10*,
815 14662. 10.1038/s41598-020-71412-0.

816 58. Franco, M., and Carmena, A. (2019). Measurement of Mitotic Spindle Angle and Mitotic Cell
817 Distance in Fixed Tissue of Drosophila Larval Brains. Bio Protoc *9*, e3432.
818 10.21769/BioProtoc.3432.

819 59. DeLay, B.D., Corkins, M.E., Hanania, H.L., Salanga, M., Deng, J.M., Sudou, N., Taira, M., Horb,
820 M.E., and Miller, R.K. (2018). Tissue-Specific Gene Inactivation in Xenopus laevis: Knockout of
821 lhx1 in the Kidney with CRISPR/Cas9. Genetics *208*, 673-686. 10.1534/genetics.117.300468.
822
823

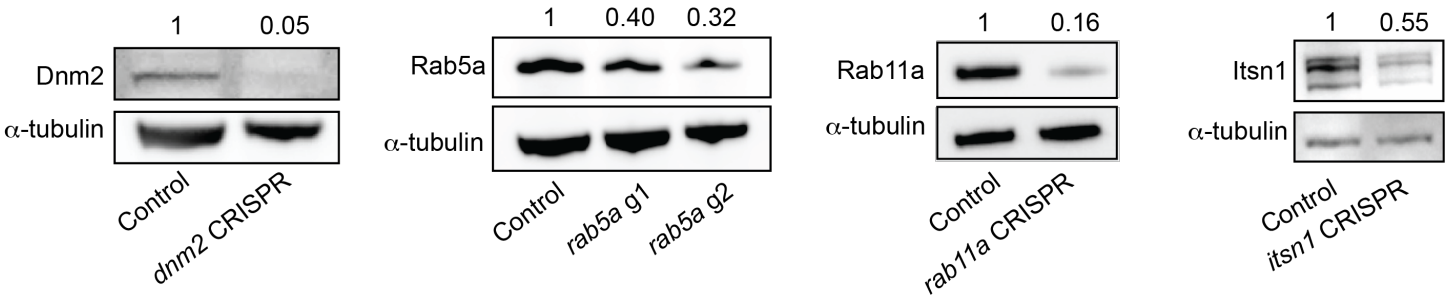

Supplemental Figure 1 (Related to Figure 1) F0 CRISPR-Cas9 editing reduces protein abundance. Western blots of Xenopus CRISPR mutants show that mutations produced by gRNAs reduce but not completely ablate the protein abundance of Dnm2, Rab5a, Rab11a, and Itsn1 in F0 *X. laevis* mutants. Relative protein abundance indicated by numbers above immunoblots, with control protein abundance normalized to 1.

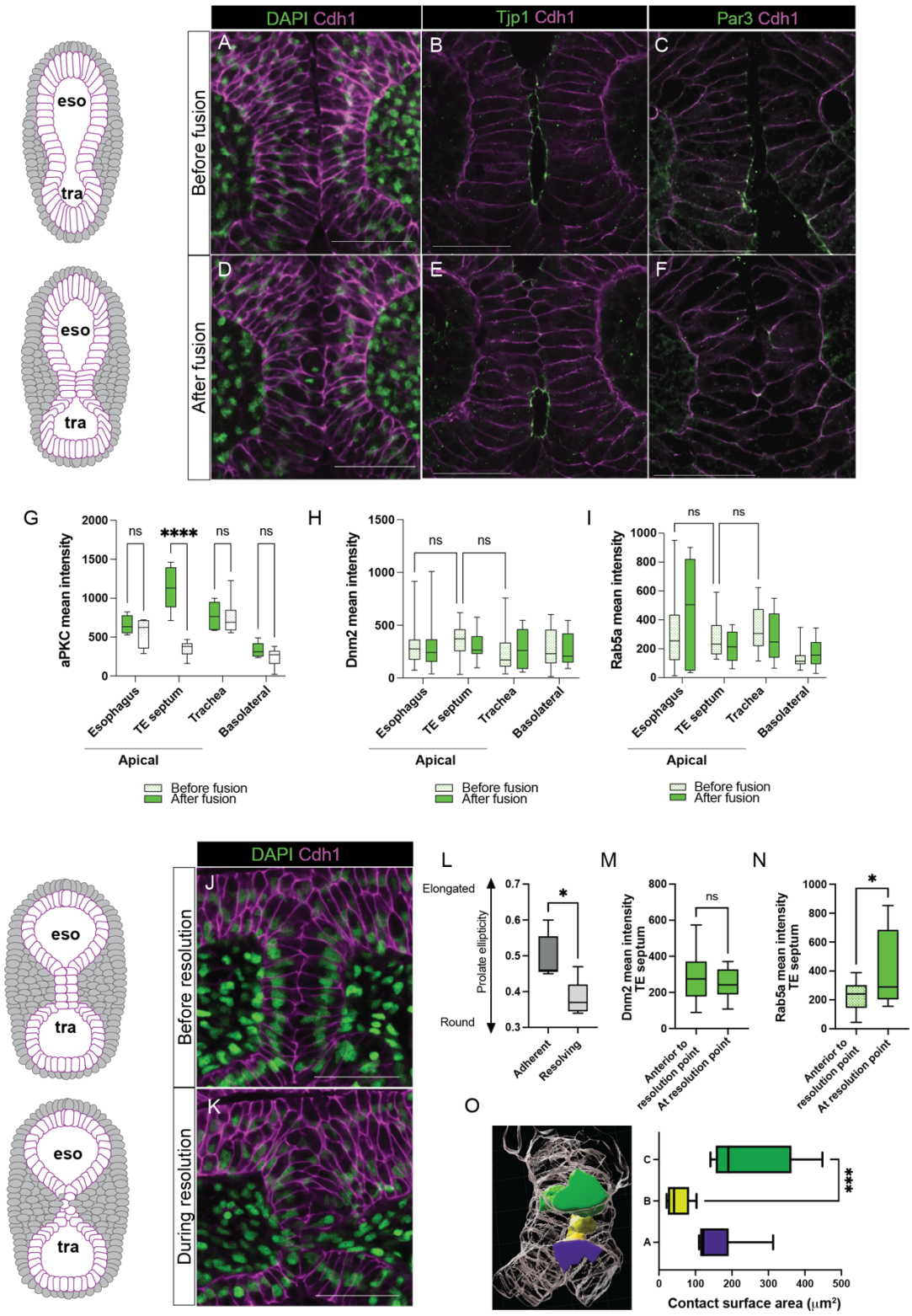

Supplemental Figure 2 (Related to Figure 2) Dynamic cell shape and polarity changes during trachea-esophageal separation. A-C) Before fusion the foregut is a pseudostratified epithelium with apical tight junctions (Tjp1) and Par3. D-F) After apical fusion, epithelial cells

837 remodel to upregulate apical E-Cadherin (Cdh1) and downregulate Tjp1 and Par3. G)
838 Quantification of aPKC downregulation after epithelial fusion (mean ± min/max, ****p<0.00001,
839 2W-ANOVA, n=6 cells per embryo, N=5 embryos). H) Quantification of Dnm2 intensity after
840 epithelial fusion (mean ± min/max, 2W-ANOVA, n=6 cells per embryo, N=5 embryos). I)
841 Quantification of Rab5a intensity after epithelial fusion (mean ± min/max, 2W-ANOVA, n=6 cells
842 per embryo, N=5 embryos). J) Before resolution of the septum, the foregut epithelium remodels
843 to a bilayered columnar epithelium with basally positioned nuclei. K) The septum resolves after
844 downregulation of E-Cadherin and integration of septum cells into either the trachea or
845 esophagus. L) Prolate ellipticity is significantly decreased in cells actively resolving in the septum
846 (mean ± min/max, *p<0.05, Student's t-test, n=6 cells per embryo, N=5 embryos). M)
847 Quantification of Dnm2 intensity before and after resolution (mean ± min/max, Student's t-test,
848 n=6 cells per embryo, N=5 embryos) N) Quantification of Rab5a intensity before and after
849 resolution (mean ± min/max, *p<0.05, Student's t-test, n=6 cells per embryo, N=5 embryos). O)
850 3D cell-surface rendering of the resolving septum with esophageal cells in green, septum cells in
851 yellow, tracheal cells in purple. Septum cells significantly decrease surface contact area with each
852 other compared to the contact between septum cells and esophageal cells (mean ± min/max, ***
853 p<0.001 1W-ANOVA, n=6 cells per embryo, N=9 embryos). Scale bars are 50 μm.
854

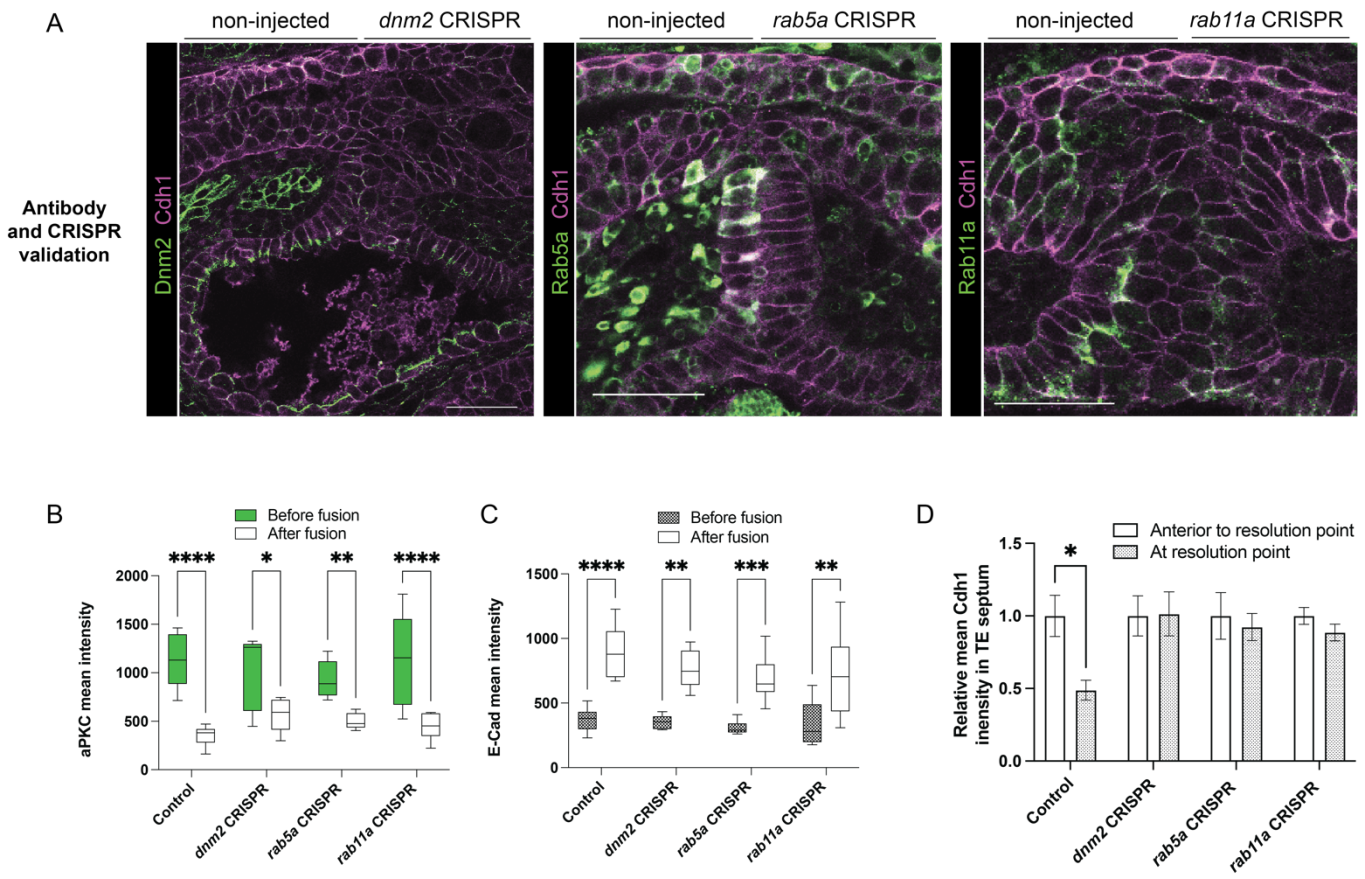

Supplemental Figure 3 (Related to Figure 3) Endosome mutants undergo epithelial fusion. A) Unilateral CRISPR injection at the 2-cell embryo stage of gRNAs against *dnm2*, *rab5a*, and *rab11a* show downregulation of fluorescence intensity compared to the control, non-injected side. B) *dnm2*, *rab5a*, and *rab11a* mutant Xenopus embryos undergo epithelial fusion at stage NF37 comparably to controls, significantly downregulating aPKC and upregulating Cdh1 (C) after epithelial fusion (mean ± min/max, Student's t-test, n=6 cells per embryo, N=5 embryos). D) Mutant TE septum epithelial cells do not downregulate Cdh1 during at the point of tissue resolution compared to controls (mean ± SEM, * $p<0.05$ 1W-ANOVA, n=6 cells per embryo, N=5-10 embryos).

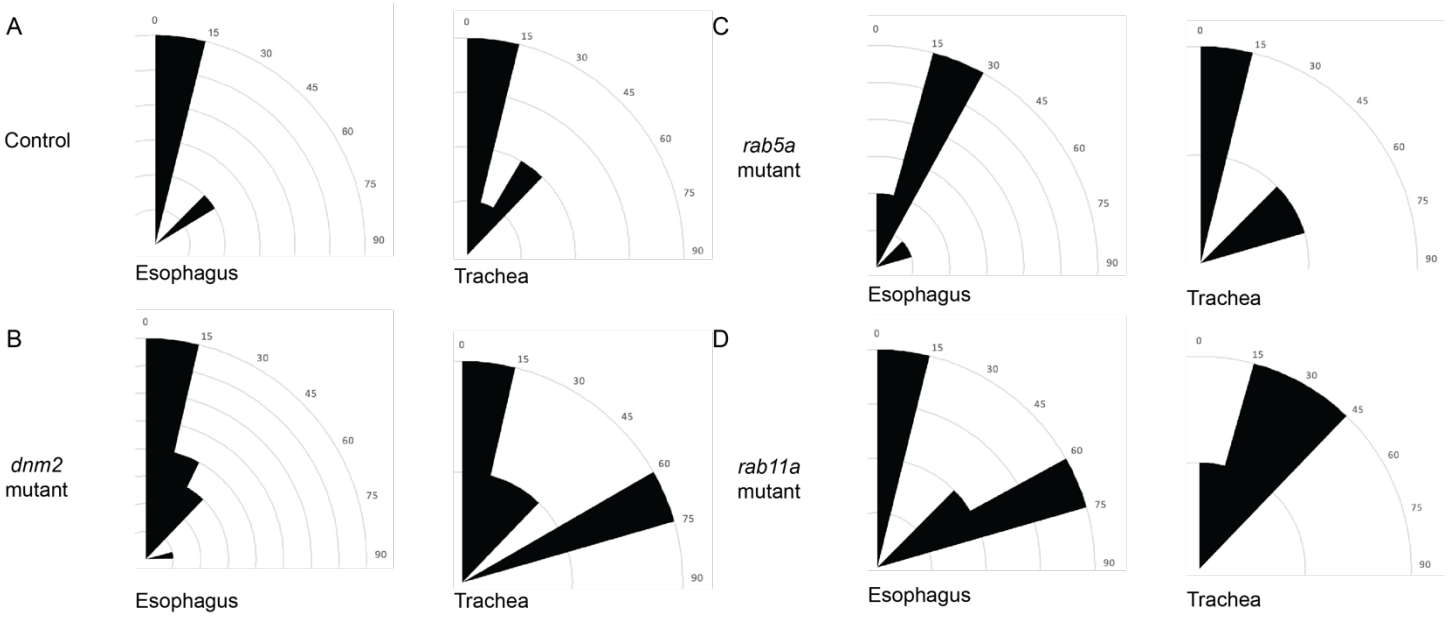

867
868
869
870 **Supplemental Figure 4 (Related to Figure 4). Mitotic spindle angles are not significantly**
871 **changed compared to controls in the trachea and esophageal epithelia of endosome**
872 **mutants.** A) Control embryo trachea and esophagus epithelia most frequently divide between 0-
873 15°C relative to the plane of the tissue. B-D) Endosome mutant trachea and esophagus epithelia
874 division angles are not significantly altered (Fisher's exact test, n.s. $p>0.05$, 3-5 cells measured
875 per embryo, 5 embryos measured per condition).
876

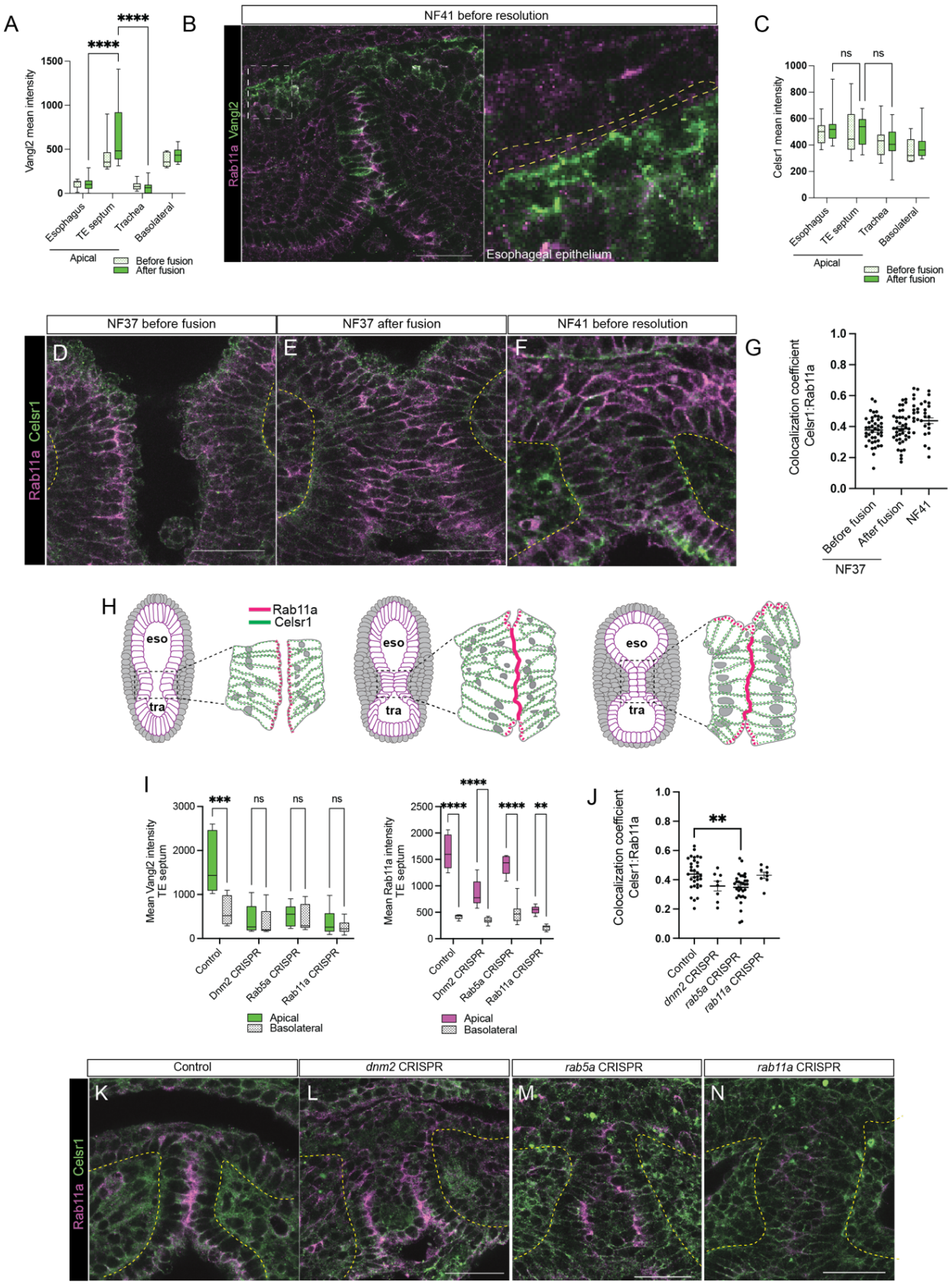
A
B
C
D
E
F
G
H
I
J
K
L
M
N
NF41 before resolution
Rab11a Vangl2
Esophageal epithelium
Vangl2 mean intensity
Esophagus
TE septum
Trachea
Basolateral
Apical
Before fusion
After fusion
Celsr1 mean intensity
ns
NF37 before fusion
NF37 after fusion
NF41 before resolution
Rab11a Celsr1
Colocalization coefficient Celsr1:Rab11a
NF37
NF41
Rab11a
Celsr1
eso
tra
Mean Vangl2 intensity TE septum
Mean Rab11a intensity TE septum
Control
Dnm2 CRISPR
Rab5a CRISPR
Rab11a CRISPR
dnm2 CRISPR
rab5a CRISPR
rab11a CRISPR

877
878

879 **Supplemental Figure 5 (Related to Figure 5) Celsr1 is localized to the periphery of cells**
880 **during tracheoesophageal separation.** A) Quantification of Vangl2 intensity before and after
881 epithelial fusion (mean ± min/max, 2W-ANOVA, ****p<0.00001. n=3-5 cells, 5 embryos analyzed).
882 B) Immunostaining of Vangl2 in the trachea and esophageal epithelium. Vangl2 is localized
883 apically in the lumen-facing esophageal epithelia but not in the more basal cell layers and does
884 not colocalize with Rab11a staining (inset). C) Celsr1 does not significantly localize with Rab11a
885 after epithelial fusion and is localized around the periphery of epithelial and mesenchymal cells
886 during tracheoesophageal development. D-F) Time course of Celsr1 immunostaining during
887 *Xenopus* trachea-esophageal morphogenesis. H) Diagrams depicting Celsr1/Rab11a localization
888 during foregut separation. I) Vangl2 intensity at the apical membrane is decreased in dnm2,
889 rab5a, and rab11a CRISPR mutants, while Rab11a remains localized to the apical membranes
890 (mean ± min/max, 2W-ANOVA, ****p<0.0001, ***p<0.001, **p<0.01, n=3-5 cells per embryo, 5
891 embryos analyzed). J-N) Celsr1:Rab11a colocalization is significantly decreased in *rab5a*
892 Xenopus mutants, but Celsr1 cellular localization is not significantly altered in *dnm2*, *rab5a*, *and*
893 *rab11a* Xenopus mutants (mean ± min/max, 1W-ANOVA, **p<0.01. n=3-5 cells, 5 embryos
894 analyzed).

***Xenopus* ortholog of patient gene**	**Protein Function**	**Frequency of alleles with damaging indels**	**Mean frequency of trachea-esophageal defect** (±SEM, n, N, p value)	**Xenopus Phenotype**
sox2^	Transcription factor	100% (germline)	100% (±0, 14, 2, p<0.0001)***	TEF – 14/14
sox2^	Transcription factor	91%	63% (±10, 17, 3, p<0.0001)***	TEF – 11/11
atp6v1b1	Intracellular transport	42-92%	44% (±19,29, 2, p=0.0024)**	TEF – 4/14 Dysmorphic esophagus – 9/14
abra^	Rho-actin regulation	20-98%	42% (±8, 30, 4, p=0.0009)**	TEF – 10/12 Dysmorphic esophagus – 4/12
itsn1^	Endocytosis, Cc42 GEF	51-92%	42% (±13, 26, 3, p=0.0038)**	TEF – 6/11 Dysmorphic esophagus – 5/11
arhgap21^	Rho family GTPase	31-76%	39% (±7, 31, 4, p=0.0006)**	TEF – 5/11 Dysmorphic esophagus – 8/11
itgb4^	Integrin adhesion, putative cargo	42-85%	34% (±8, 45, 5, p=0.0063)**	TEF – 9/13 Dysmorphic esophagus – 4/13
lamb4	Laminin subunit	26-76%	30% (±19, 32, 3, p=0.0121)*	TEF - 9/10 Dysmorphic esophagus – 1/10
celsr2^	Cell polarity, putative cargo	43-75%	28% (±5, 30, 2, p=0.0041)**	TEF - 6/8 Dysmorphic esophagus – 2/8
rasal2	Ras GTPase-like	40-81%	27% (±2, 22, 3, p=0.0005)***	TEF - 5/6 Dysmorphic esophagus – 5/6
ap1g2^	Endocytosis	35-87%	20% (±3, 40, 5, p=0.0038)**	TEF – 7/7
rapgef3^	Ras signaling	39-87%	17% (±3, 32, 3, p=0.0360)*	TEF – 4/4 Dysmorphic esophagus – 2/4
ap3d1	Intracellular transport	70-90%	15% (±7, 21, 2, p=0.0808)	-
cldn10	Tight junctions	85-86%	14% (±7, 34, 3, p=0.1106)	-
pcdh1^	Cell adhesion, putative cargo	60-76%	13% (±7, 39, 3, p=0.1361)	-
itpr1	Inositol triphosphate receptor	93%	8% (±14, 25, 3, p=0.4262)	-
rasa2	Ras GTPase	60-93%	9% (±8, 38, 4, p=0.1950)	-
add1	Cytoskeleton	89%	5% (±5, 37, 3, p=0.6608)	-
rab3gap2^	Endocytosis	81%	5% (±6, 31, 3, p=0.5948)	-
arhgap17^	Rho signaling	78%	4% (±4, 31, 5, p=0.7341)	-
akap13	Rho guanine exchange factor	85%	6% (±6, 29, 3 p=0.5165)	-
tyr (control)	Pigmentation	n/d	2% (±2, 36, 6)	-

Endosome genes	Protein Function	Frequency of alleles with damaging indels	Mean frequency of trachea-esophageal defect (±SEM, n, N, p value)	Xenopus Phenotype
X.t. dnm2	Endocytosis	62-98%	71% (±9, 18, 2, p<0.0001)***	TEF – 7/18 Dysmorphic esophagus – 5/18
X.t. rab5a	Early endosome GTPase	45-75%	50% (10, 1)	TEF – 4/10 Dysmorphic esophagus – 2/10
X.t. rab11a	Recycling endosome GTPase	42-92%	39% (±1, 13, 2, p=0.0003)***	TEF – 1/13 Dysmorphic esophagus – 5/18
X.l. dnm2.L + *dnm2.S*	Endocytosis	47-93% (L) 50-94% (S)	95% (±4, 22, 4, p<0.00001)****	TEF – 19/20 Dysmorphic esophagus – 11/20
X.l. rab5a.L + *rab5a.S*	Early endosome GTPase	45-74% (L) 46-93% (S)	88% (±7, 32, 5, p=0.0002)***	TEF – 24/28 Dysmorphic esophagus – 8/28
X.l. rab11a.S	Recycling endosome GTPase	65-95%	75% (±14, 12, 3, p=0.0065)**	TEF - 7/9 Dysmorphic esophagus – 3/9
X.l. vangl2.L + *vangl2.S*	Cell polarity, putative cargo	56-95% (L) 46-81% (S)	32% (±13, 22, 2, p=0.05)	TEF – 5/7 Dysmorphic esophagus – 1/7
X.l. celsr1.L + *celsr1.S*	Cell polarity, putative cargo	77-95% (L) 84-93% (S)	42% (±9, 17, 3, p=0.0096)**	TEF - 6/7 Dysmorphic esophagus – 1/7

Supplemental Table 1.

^reported in Zhong et al., HGG Advances 20222
TEF – trachea-esophageal fistula
SEM – standard error of the mean, n=number of embryos assayed, N=number of independent experiments
p value determined by unpaired Student's t-test compared to *tyr* controls

Gene	Patient genotype-phenotype	Reference
CELSR1	DNV – EA CNV – feeding difficulties in infancy, abnormal esophagus morphology, respiratory distress	Zhang et al., 2020[48] DECIPHER 1937 (+10 patients), 254458, 397368 (+3 patients)
CELSR2	DNV – EA/TEF	Zhong et al., 2022[21]
VANGL1	CNV– feeding difficulties in infancy	DECIPHER 263708
VANGL2	CNV – laryngeal stenosis, respiratory insufficiency, feeding difficulties in infancy	DECIPHER 285906, 289199, 263708

Supplemental Table 2.

DNV – *de novo* variant; CNV – copy number variant; data taken from the DECIPHER database https://www.deciphergenomics.org